

FEA MODELING OF A TRIBOMETER'S
PIN AND DISK INTERACTION

FEA MODELING OF A TRIBOMETER'S PIN AND DISK INTERACTION

By

HAOYU LI, B.Eng

A Thesis

Submitted to the School of Graduate Studies

in Partial Fulfillment of the Requirements

for the Degree

Master of Applied Science

McMaster University

© Copyright by Haoyu Li, Sept 2012

MASTER OF APPLIED SCIENCE (2012)

McMaster University

(Mechanical Engineering)

Hamilton, Ontario

TITLE: FEA Modeling of a Tribometer's Pin and Disk Interaction

AUTHOR: Haoyu Li

SUPERVISOR: Dr. Stephen Veldhuis, Dr. Peidong Wu

Department of Mechanical Engineering

McMaster University

NUMBER OF PAGES: x, 80

Abstract

A bench scale tribometer, developed at the McMaster Manufacturing Research Institute (MMRI) was designed for mimicking the friction and wear conditions on the rake face of a metal cutting tool. It provides insight into the performance of cutting tools operating under high stress and high temperature machining conditions. It saves test material costs, reduces machine downtime for testing, increases the number of test replicates and effectively adds a reliable testing tool to characterize metal cutting operations.

A detailed investigation into the stress distribution, temperature profile and indentation pattern has been performed in order to verify the ability of the device to capture the machining environment and to gain a better understanding of the friction effects and wear conditions. The investigation used finite element analysis to simulate the MMRI's tribometer with the FEA results compared to the experimental results. This data was then used to tune the operating conditions of the tribometer to improve its ability to simulate the machining environment.

Acknowledgements

I would like to express my heartfelt gratitude to my supervisors, Dr. Wu and Dr. Veldhuis for their motivation, encouragement and guidance, in helping me throughout the research. The opportunities given by them in allowing me to be involved in the industrial project and the conference is deeply appreciated.

I would also like to specially thank Dr. Ng, Dr. Koshy and Dr. Fox-Rabinovich who offered valuable expertise and insightful suggestions.

I would like to specially thank Mr. Jeremy Boyd and Mr. Andrew Biksa for their help on my research and providing experimental data.

Among my colleagues, I would like to thank Mr. Boke, Mr. Huamiao Wang, Mr. Jin Peng, Mr. Hua Qiao and Ms. Amy Short for sharing their ideas and support.

Lastly, I would like to thank my parents, Baohua Li and Aihua Ren, as well as my wife, Lin Xu, for giving me consistent love and encouragement. Without them this would not be possible.

Table of Contents

Acknowledgements	iiv
List of Figures	vii
List of Tables	x
Chapter 1. Introduction.....	1
1.1 Background	1
1.2 Objectives.....	2
Chapter 2. Literature Survey	3
2.1 Metal Cutting	3
2.1.1 Friction in Metal Cutting	4
2.2 Tribometer	11
2.3 FEA modelling of tribological test	18
2.3.1 Normal contact.....	18
2.3.2 Sliding contact.....	25
Chapter 3. System Configuration	28
3.1 MMRI Tribometer	28
3.2 Pin & Disk.....	29
3.3 Testing Procedure	30
Chapter 4. Numerical Model.....	31
4.1 Material Constitution Model	31
4.2 Friction Models	33
4.3 Contact Algorithm	34

4.4	FEA modeling.....	36
4.4.1	2D modelling of indentation.....	36
4.4.2	3D modelling of indentation.....	43
Chapter 5.	Results and Discussions.....	45
5.1	Comparison between FEA and MMRI experimental results	45
5.1.1	2D simulation	45
5.1.2	3D simulation	56
5.2	Boundary conditions effects	59
5.2.1	Force controlled boundary condition	59
5.2.2	Displacement controlled boundary condition.....	63
5.3	Temperature effects	67
5.4	Soft pin indenting on hard disk	70
Chapter 6.	Conclusions.....	73
Chapter 7.	Conclusions.....	74
Chapter 8.	Bibliography.....	75

List of Figures

Figure 2-1: Tool-workpiece interact diagram	3
Figure 2-2: three regimes of solid friction	5
Figure 2-3: variation of shear and normal stress on rake face	6
Figure 2-4: Temperature distribution inside the tool and workpiece	8
Figure 2-5: effect of cutting speed on coefficient of friction on tool rake face.	10
Figure 2-6: Shaw's test apparatus.....	11
Figure 2-7: Variation of τ and σ for unlubricated tests	12
Figure 2-8: Shuster's test apparatus.....	13
Figure 2-9: comparison between the COF and Flank wear for different coating. 14	
Figure 2-10: Stress distributions at the surface	20
Figure 2-11: Contours of von Mises equivalent stress.....	23
Figure 2-12: Effect of contact friction on the indentation profile.....	24
Figure 2-13: Schematic of two solids in a sliding contact	25
Figure 2-14: Normalized stress σ_x/p_0 along the x-axis.....	26
Figure 3-1: Illustration of the MMRI Tribometer.	28
Figure 3-2: Pin and disk.....	29
Figure 4-1: Stick and slip regions for Coulomb's friction.....	33
Figure 4-2: Normal stress distribution.....	35
Figure 4-3: 2D model of the tribometer.....	36
Figure 4-4: overall mesh & mesh details near the contact zone.	37
Figure 4-5: Comparison of contact area.	39

Figure 4-6: Comparison of the normalized normal stress at the contact surface	40
Figure 4-7: Comparison of the normalized normal stress along the axis of symmetry.....	40
Figure 4-8: Comparison of the Load vs. Displacement Curve	41
Figure 4-9: 3D model of the tribometer.....	43
Figure 4-10: Comparison of Load Displacement Curve between 2D and 3D simulation.	44
Figure 5-1: Indentation diameter under different loads for 2D simulation	46
Figure 5-2: Contours of Von Mises stress distribution.	50
Figure 5-3: Contours of equivalent plastic strain distribution.	52
Figure 5-4: Contours of normal stress distribution.	54
Figure 5-5: Contours of normal stress distribution.	55
Figure 5-6: Reaction torque and indentation diameter at different temperature .	56
Figure 5-7: Shear Stress Distribution	58
Figure 5-8: Two boundary conditions, Force control & Displacement control....	59
Figure 5-9: Indentation Depth Curve for different coefficients of friction	60
Figure 5-10: Contact Diameter Curve for different coefficients of friction	61
Figure 5-11: Coefficient of Friction Comparison	63
Figure 5-12: normal force curve for different coefficient of friction.....	64
Figure 5-13: Normal Force Curve for Different Indentation Depth	65
Figure 5-14: friction calculated using the force, before rotation & after rotation..	66
Figure 5-15: Indentation Depth curve for surface friction of 0.2.....	68

Figure 5-16: FEA results for friction coefficient of 0.2	69
Figure 5-17: Normal stress distribution.....	70
Figure 5-18: Von Mises Stress Distribution.	71
Figure 5-19: Equivalent Plastic Strain Distribution.....	71
Figure 5-20: Calculated COF vs. Input COF.....	72

List of Tables

Table 4-1: Johnson-Cook Parameters for Ti6Al4V	31
Table 4-2: Mechanical Properties of Ti6Al4V	32
Table 4-3: Comparison of Maximum stresses and contact radius	42

Chapter 1. Introduction

1.1 Background

Tribological failure is one of the most common problems that limit productivity. During a machining operation, the contact zone between the metal cutting tool and workpiece material will begin to wear which leads to failure of the tool and low quality of products. Many studies have been done to characterize the tribological interactions between metal cutting tools and workpieces during industrial machining applications to reduce wear. Early studies done by Shaw et al. [1960] proposed a bench scale test to simulate metal cutting on the rake face of a tool. His work was performed under near zero velocity seizure conditions, which isolated the plastic adhesive mechanism from the ploughing component in the seizure zone of the rake face. Similar work done by Shuster et al.[1997] included metal cutting temperatures in the test which captured the friction and wear conditions of the cutting tool operations better. A tribometer [Biksa, 2010] developed at the McMaster Manufacturing Research Institute (MMRI) took the positive design aspects of the two prior works and combined them into a unique system. At the same time, a finite element analysis was performed to simulate the MMRI's tribometer with the FEA results being compared to the MMRI experimental results. This data is then used to tune the operating conditions of the tribometer, such as establishing various boundary conditions for testing, and

studying the impact of a pin-disk material reversal, in order to improve its ability to simulate the machining environment. A reversal of materials for the pin and disk was considered in an attempt to simplify the preparation of the components needed for the test.

1.2 Objectives

The objective of this project was to build a Finite Element Model of the MMRI tribometer in order to:

1. map the stresses and indentation profiles to more accurately calculate COF,
2. examine alternative testing methods for calculating COF, and
3. use the FE model as an assistive tool for the MMRI tribometer.

Chapter 2. Literature Survey

2.1 Metal Cutting

Metal cutting is one of the most important material removal processes in manufacturing. It involves the removal of macroscopic chips which have a thickness from about 10^{-3} inch to 10^{-1} inch. As shown in Figure 2-1, during the machining operation, the workpiece material is plastically deformed by the cutting tool. There are three main regions that plastic deformation occurs: the primary shear zone on the shear plane, the secondary shear zone along the rake face of the tool and the tertiary deformation zone (or rubbing zone) on the flank face of the cutting tool.

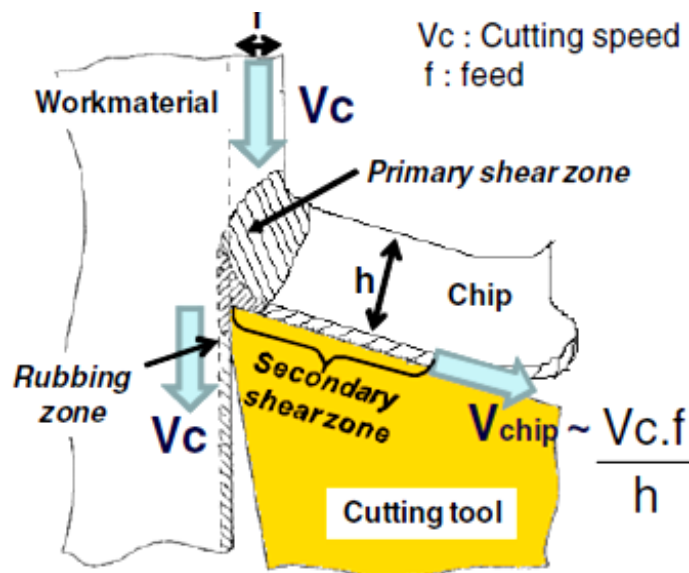


Figure 2-1: Tool-workpiece Interact Diagram [Ghosh & Malik, 1985]

In the primary shear zone, the workpiece material will undergo a substantial amount of simple shear and extremely high strain rate as it crosses the shear plane. This is the area where the chip is formed. In the secondary shear zone, the chip formed in the primary shear zone will slide along the tool rake face. This is the major zone of tool-chip friction interaction, which causes wear to the tool. Therefore, the main area of our study focused on the friction behaviour in the secondary shear zone along the tool rake face.

2.1.1 Friction in Metal Cutting

Before delving into friction behaviour between the tool and workpiece in metal cutting, it is important to outline the field of the classic friction. Friction is the force that resists motion between two surfaces sliding against each other, and it is the major cause of wear. Amontons-Coulomb Friction Law is the most well-known and commonly used theory. It describes the friction coefficient as the relationship between the tangential friction force F_f and the normal force F_n :

$$\mu = \frac{F_f}{F_n} \quad (1)$$

where μ is the coefficient of friction. The law also states that the coefficient of friction is independent of the friction force, the sliding speed and the contact area.

However, at the microscopic level, all finished surfaces are found to have irregularities. Normally, when two bodies are in contact, only a portion of the apparent area of contact (A_A) is actually touching on both surfaces. This causes the real area of contact (A_r) to be much smaller than the apparent area of contact

as shown in Figure 2-2. As the load increases, more and more irregularities will make contact and plastically deformed, causing the real area of contact increase.

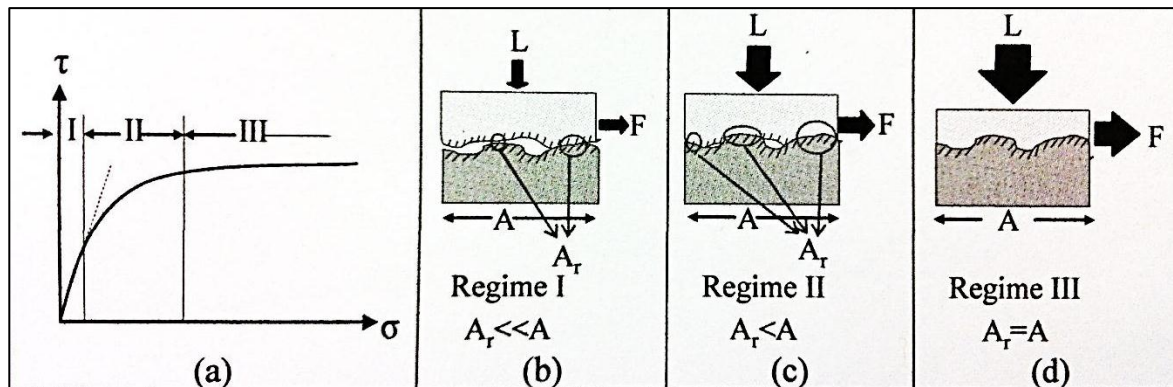


Figure 2-2: Three Regimes of Solid Friction [Shaw, 2005].

Shaw et al. [1960] suggested that the field of friction could be divided into three general regimes: a lightly loaded regime, a transition regime between the lightly loaded and heavily loaded regime, and the heavily loaded regime as shown in Figure 2-2. In regime I, due to the roughness of the surface, the real area of contact (A_r) is much less than the apparent area of contact (A_A) under lightly loaded condition. This is the regime where classical friction, Coulomb's friction law holds. Regime III is the deformation friction regime, where the load is high enough that the real area of contact is the same as the apparent area of contact. As a result, there will be subsurface plastic flow and internal shear stress occurring inside the soft material. At the same time, the change in load does not change the contact area further, so in this case, the shear stress is independent of normal stress. Regime II is the transition region between regime I and regime

III. For this regime, the real area is approaching the apparent area, and the coefficient of friction decreases with an increase in load. According to Shaw et al. [1960], surface sliding is accompanied by some subsurface plastic flow in this regime, and it corresponds to the situation on the tool rake faces in the metal cutting process.

In metal cutting, friction plays a very important role on both the rake face and the flank face of the cutting tool. In this application, the tool experiences extremely high stress due to the high normal and high sliding velocity. The stress distribution along the tool-chip interface proposed by Zorev [1963] in Figure 2-3 has been widely used as a model of the frictional behaviour in metal cutting.

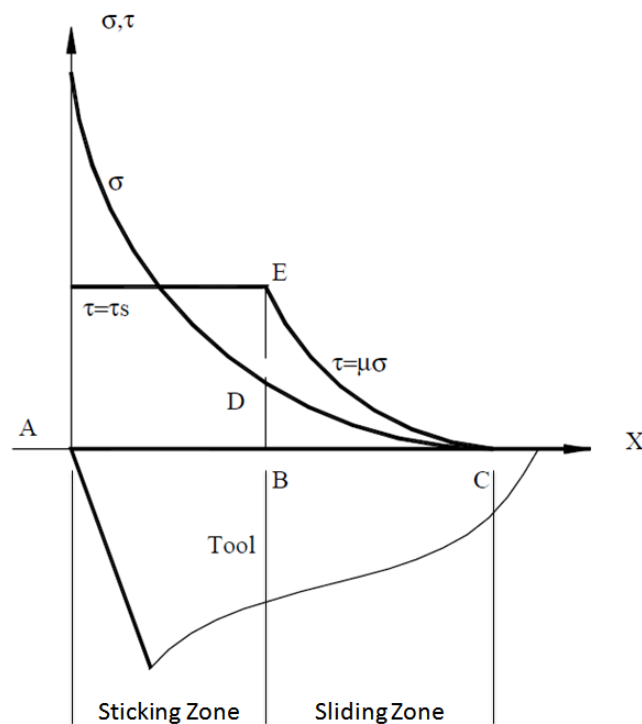


Figure 2-3: Variation of Shear and Normal Stress on Rake Face [Zorev, 1963]

In this Figure, the normal stress is highest at the tip of the tool in the sticking zone and decays along the rake of the cutting tool. According to Trent and Wright [2000], the mean normal stress during machining materials like carbon steel and titanium can vary from 0.5 to 1.6 GPa in the sticking zone. Work done by Boothroyd [Boothroyd & Geoffrey 1985] shows that the maximum normal stresses at the tool tip could reach as high as 3.5 GPa. Thus, a typical normal stress is in the range of 0.5-3.5 GPa in the sticking zone of the tool rake face. The shear stress is independent of the normal stress and remains constant throughout the sticking region. According to Trent [Trent & Wright, 2000] and Chandrasekaran [Chandrasekaran & Kapoor, 1965], the shear stress was found to be about 15-50% of the normal stress in the sticking zone. In the sliding region, shear stress decreases with the normal stress, and it is found to be a function of the normal stress.

Between the sticking and sliding region is where the adhesion occurs, stick and slip phenomenon is observed between the workpiece and cutting tool [Shaw, 2005]. As the normal stress decreases, less adhesion occurs and the condition will approach that of lightly loaded regime in the sliding region, where the Coulomb's law of friction will hold. Zorev's model is just an approximation of what is happening at the tool face during metal cutting. To simplify the contact region, it is common to only consider adhesion [Shaw, 2005] or a combination of sliding contact and sticking contact [Stephenson, 1997] in an analysis of metal cutting.

2.1.2 Temperature in Metal Cutting

During the metal cutting process, both the tool and the workpiece will also experience an extremely high temperature, due to the thermal energy generated during the metal cutting operation. According to Shaw [2005], there are two major sources of thermal energy in metal cutting: 1) in the primary shear zone and 2) in the secondary shear zone. In the primary shear zone, the work done by deforming and shearing the workpiece to form the chip is the major source of the heat generated. In the secondary shear zone, friction between the tool and workpiece, as well as the subsurface plastic deformation are considered as substantial sources of thermal energy generated.

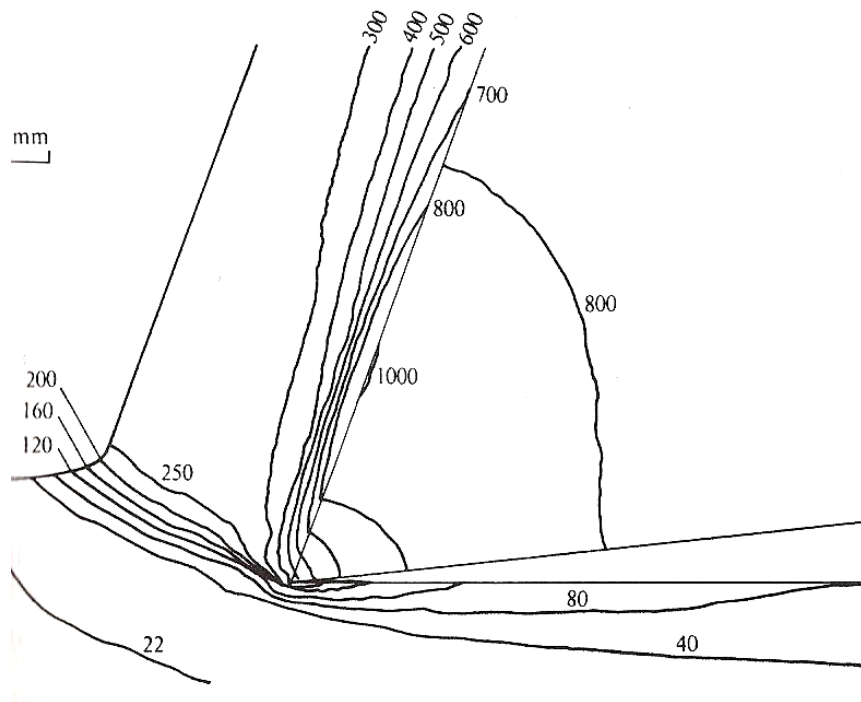


Figure 2-4: Temperature Distribution inside the Tool and Workpiece [Shaw, 2005]

Figure 2-4 shows a typical temperature distribution inside the tool and workpiece during a metal cutting process. As the chip first enters the primary shear zone, the shear deformation causes thermal energy to heat the chip. Then the portion of the chip that rubs against the rake face will continue to be heated due to friction. As a result, the maximum temperature is developed at the rake face of the cutting tool, some distance away from the tool nose, and the higher temperature is found on the rake side than the opposite side for the chip. The average temperature rise at the rake face can be obtained by dimensional analysis [Schey, 1983]:

$$\Delta T = E \left(\frac{vt}{k\rho C} \right)^{1/2} \quad (2)$$

where E is specific cutting energy, v is cutting speed, t is depth of cut, k is heat conductivity, ρ is density, and C is specific heat of the workpiece material. This shows that both the cutting speed and depth of cut are of equal importance relative to the temperature. Higher cutting speed will result in a higher average temperature rise at the rake face.

Temperature also has a great impact on the mean coefficient of tool face friction during the metal cutting process as shown in Figure 2-5. According to Zorev's work, the mean coefficient of friction initially increases with an increase in cutting speed (or temperature). This is because the increase in the adhesive bonding dominates the reduction of the shear strength of the workpiece material as the temperature increases. Then the mean coefficient of friction reached a maximum and decreased continuously with a further increase in cutting speed.

This is caused by the domination of the shear strength reduction over the adhesive bonding factor [Zorev, 1966].

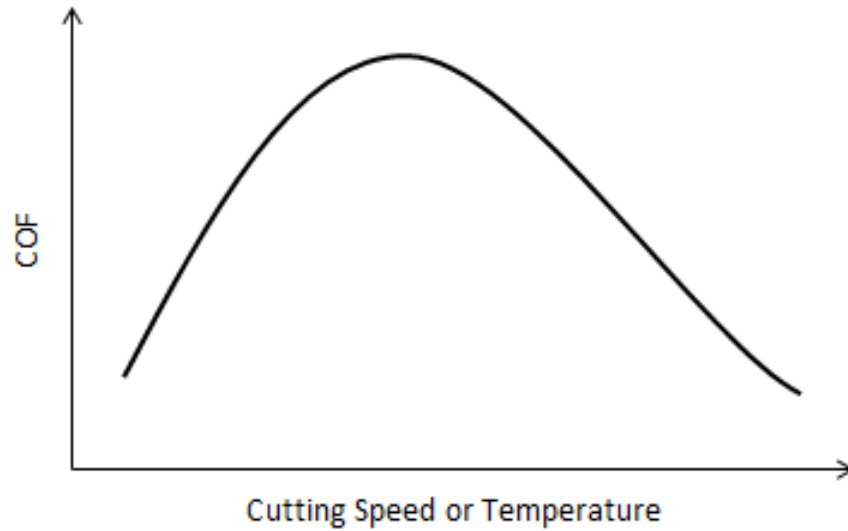


Figure 2-5: Effect of Cutting Speed on Coefficient of Friction [After Zorev, 1966].

2.2 Tribometer

Industrial testing of the tooling condition can be expensive and time consuming. It involves loss of manpower, downtime of machines and consumption of material. Therefore, many bench scale systems focusing on the tool-workpiece interaction have been developed in recent year to simulate the metal cutting condition with a relatively lower cost. The first was proposed by M.C Shaw et al. [1960]. His bench scale system was based on a modified Brinell hardness test, which focused specifically on isolating the plastic flow in the seizure zone of the tool rake face. A sketch of Shaw's test apparatus is in Figure 2-6.

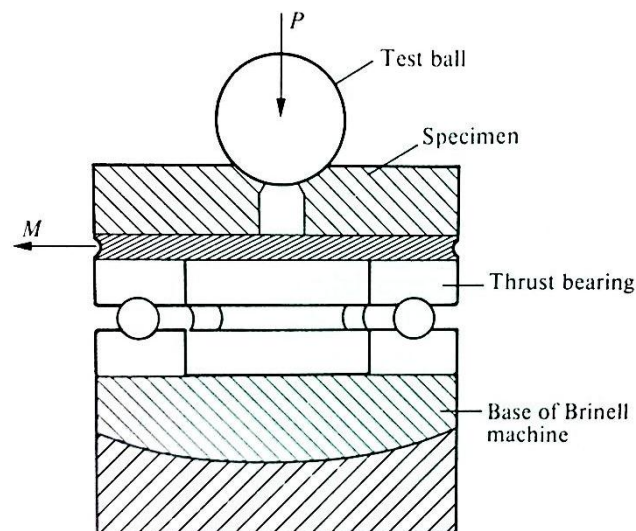


Figure 2-6: Shaw's Test Apparatus [Shaw et al. 1960]

In this figure, a spherical test ball made from tooling material is first plastically loaded against a flat disk made from workpiece material under extremely high pressure. This made the real area of contact between them approach the apparent area of contact, similarly to the condition in the seizure

zone region of the tool rake face. Then the disk is rotated at near zero velocity to simulate the plastic adhesive mechanism in the seizure condition. This can be shown by the shear stress versus normal stress graph for sliding with mild steel in Figure 2-7.

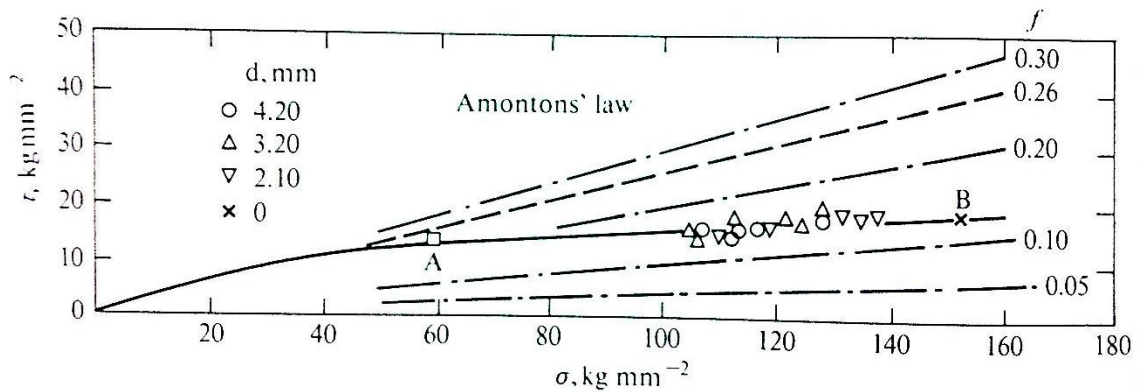


Figure 2-7: Variation of Shear Stress and Normal Stress [Shaw et al. 1960]

In this graph, the mean shear stress remains relatively constant after the normal stress reached about 100 kgmm⁻² (1GPa), showing similar mechanical behaviour to the seizure zone of the tool rake face. As a result, Shaw was able to successfully isolate the adhesive friction condition on the rake face of a cutting tool by using this bench scale apparatus.

The mean normal stress at the contact interface is also found to have an upper limit. According to Bowden and Tabor [1950], when a hard indenter is pressed against a soft workpiece material during a Brinell hardness test, the mean normal stress will increase as the load increases, until it reaches approximately 3 times of the yield stress (Y) of the soft material. This is the case when the full plasticity of the workpiece material is obtained, and the stress of $3Y$

is referred to as the indentation hardness of the softer material [Rabinowicz, 1995]. This finding has also been verified by numerical methods, which will be discussed in the next section.

Although Shaw was able to isolate the adhesive friction condition, he did not simulate the temperature effect in his work. Later, L. S. Shuster constructed a similar setup like Shaw's, but included the temperature effect in the system by incorporating a resistance heater.

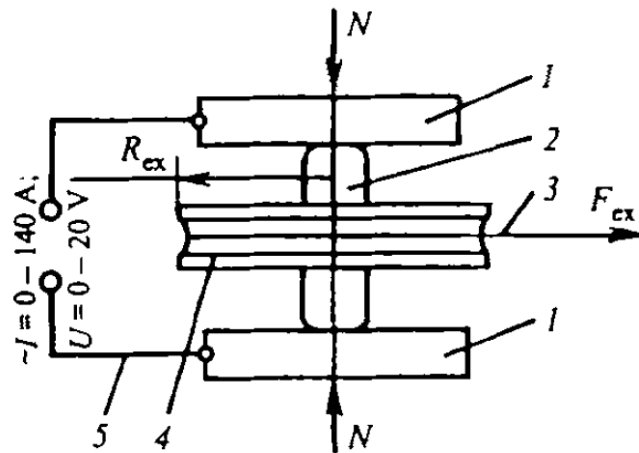


Figure 2-8: Shuster's Test Apparatus: 1) disk specimens made of a soft material; 2) indenter specimen with spherical end faces made of a hard material; 3) drive cable; 4) disk; 5) circuit for electric-contact heating of the friction contact. [Korotkov et al. 1997]

As shown in Figure 2-8, the spherical indenter is pressed by two plane-parallel specimens which rotate about its axis under a heavily loaded force, which could generate similar normal stresses as Shaw's setup. Electrical resistance heating method is used to heat the contact surface up to 1000°C to create similar temperature condition as those experienced on the tool rake face during machining. Based on this apparatus, Shuster was able to plot the evolution of the coefficient of friction with temperature for a constant load

[Korotkov et al. 1997]. Later, some collaboration work of the MMRI with Dr. Shuster is done by Dr. G. Fox-Rabinovich shows that the trends in coefficient of friction agree with the metal cutting wear trends. The coefficient of friction between the pin and the disk at different temperature is firstly calculated, and then the trend in friction is compared with the metal cutting wear trends using the same material pair.

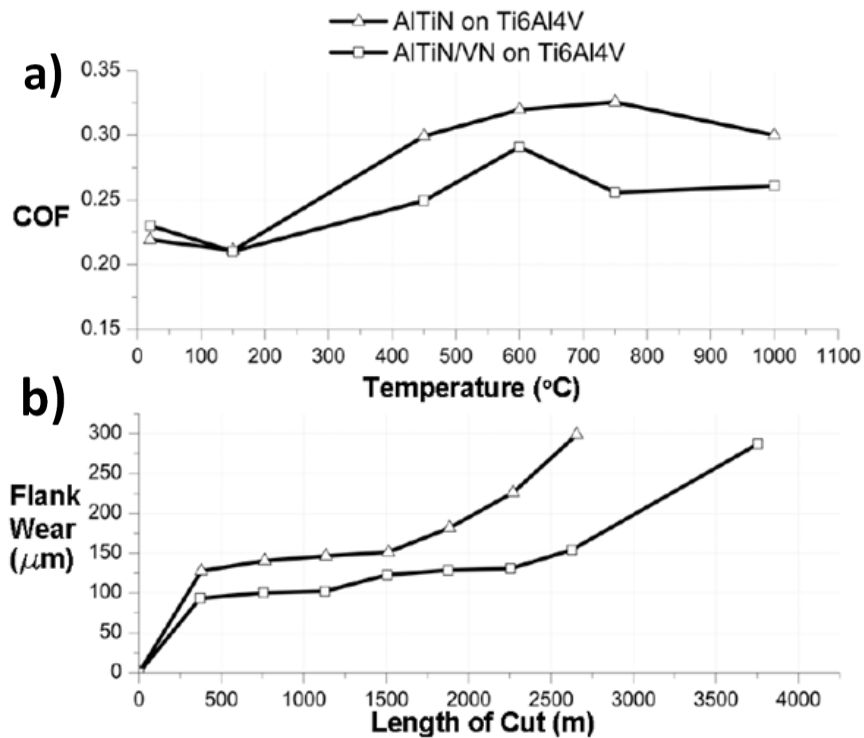


Figure 2-9: Comparison between COF and Flank wear for Different Coatings [Biksa et al. 2010].

Figure 2-9(a) shows the coefficient of friction from Shuster's tribometer as a function of temperature for a tungsten carbide pin with a different coating sliding against Ti6Al4V disk, and Figure 2-9(b) is the MMRI machining data for the same material pair. The material pair with lower coefficient of friction exhibits lower

flank wear and longer tool life. This improved tool life is attributed to the reduced level of friction as measured on Shuster's tribometer.

Based on the two prior works of Shaw and Shuster, a tribometer simulating the adhesive mechanism in metal cutting tool was constructed at the MMRI and a COF equation is derived by Biksa [2010] to measure the tool workpiece friction.

$$COF = \frac{\tau}{\sigma} = \frac{3M_{TOT}}{F_N D_{IND}} \quad (3)$$

where τ is the mean shear stress which is given by

$$\tau = \frac{3M_{TOT}}{4\pi R_{IND}^3} \quad (4)$$

and σ is the mean normal stress which is given by

$$\sigma = \frac{F_N}{\pi R_{IND}^2} \quad (5)$$

In these equations, M_{TOT} is the torque moment applied to the pin from friction, F_N is the normal load and D_{IND} is the outer diameter of the indentation print on the disk.

Therefore, the tribometer constructed in MMRI was designed to establish a trend between the measured COF and the flank wear similar to the trend obtained by Shuster. This tribometer setup is the main focus of this research and it will be discussed in detail in the next chapter.

The MMRI tribometer design has the following key advantages that make it a very useful bench scale apparatus for mimicking the adhesive mechanism in metal cutting tool:

- Due to the fact that industrial testing could be very expensive and time consuming, the usage of the tribometer is able to save test material costs, reduce machine downtime cost for testing, and complete more tests in a set period of time.
- Because the input parameter for tribometer testing is force and temperature, the effects of normal stress and temperature could be tested separately.
- The coefficient of friction obtained from the tribometer could be used as a parameter for comparing and studying the tool wear.
- Various coatings and tooling material could be examined by the tribometer for preliminarily selecting the combination of tool and workpiece for further industrial testing on real machines.

Despite the fact that the tribometer could simulate some important aspects of metal cutting, there are also some limitations. For example, the tribometer could not simulate the effects of different metal cutting parameters (i.e. rake angle, clearance angle, feed rate, depth of cut, width of cut, nose radius cutting edge radius, etc.) chip formation or the dynamic aspects of metal cutting such as chatter [Biksa, 2010]. Also, the tribometer could only capture the adhesive mechanism on the tool face, which is only one part of the total wear mechanisms

experienced during metal cutting operations. Moreover, it is also difficult to generate a temperature, stress and indentation profile directly from the tribometer, so numerical modelling of the tribometer is necessary to more accurately calculate the coefficient of friction.

2.3 FEA modelling of tribological test

Numerical modelling of spherical contacts has been done intensively for the past hundred years. Most of the research focused on the normal and linear sliding contacts of elastic and elastic-plastic solids. By far, numerical modeling of the tribometers discussed in Section 2.2 has never been done. However, since the tribometers involves both indentation and rotational sliding behaviour, the numerical modelling of the tribometers could be analysed separately. Thus, the numerical modelling of the normal contact and sliding contacts will be discussed in the following section.

2.3.1 Normal contact

The analysis of the stresses at the contact of two elastic solids was first studied by Hertz in 1882. Based on his Hertzian contact theory [Hertz, 1882], stress profile relating to the spherical, cylindrical and conical contacts is well defined. This theory was based on four assumptions, which were summarized by Johnson [1985]: 1) the surfaces are continuous and non-conforming, 2) the strains are small and within the elastic limit, 3) Each body can be considered as an elastic half space, and 4) the surfaces are frictionless. The pressure distribution at a certain distance r , from the center axis is given by:

$$p = p_0 \{1 - (r/a)^2\}^{1/2} \quad (6)$$

with

$$p_0 = \frac{3}{2}p_m = \frac{3P}{2\pi a^2} = \sqrt[3]{\frac{6PE^{*2}}{\pi^3 R^2}} \quad (7)$$

and

$$a = \sqrt[3]{\frac{3PR}{4E^*}} \quad (8)$$

Here, p_0 is the maximum pressure, a is the contact radius, P is the applied normal load and p_m is the mean contact pressure ($p_m = P/\pi a^2$). R is the effective curvature,

$$\frac{1}{R} = \frac{1}{R_1} + \frac{1}{R_2} \quad (9)$$

where R_1 and R_2 are the radii of the two elastic solids, and E^* is the effective modulus,

$$\frac{1}{E^*} = \frac{1-\nu_1^2}{E_1} + \frac{1-\nu_2^2}{E_2} \quad (10)$$

where ν_1 and ν_2 are the Poisson's ratio and E_1 and E_2 are the Young's Modulus of the two elastic solids.

Thus, for a give normal load, dimension and material properties of the contact pair, the pressure distribution between them could be obtained from the above equations. Based on this Hertzian pressure distribution, the different stress components within the two solids are calculated by Morton [Morton & Close, 1922] and Hamilton [Hamilton & Goodman, 1966].

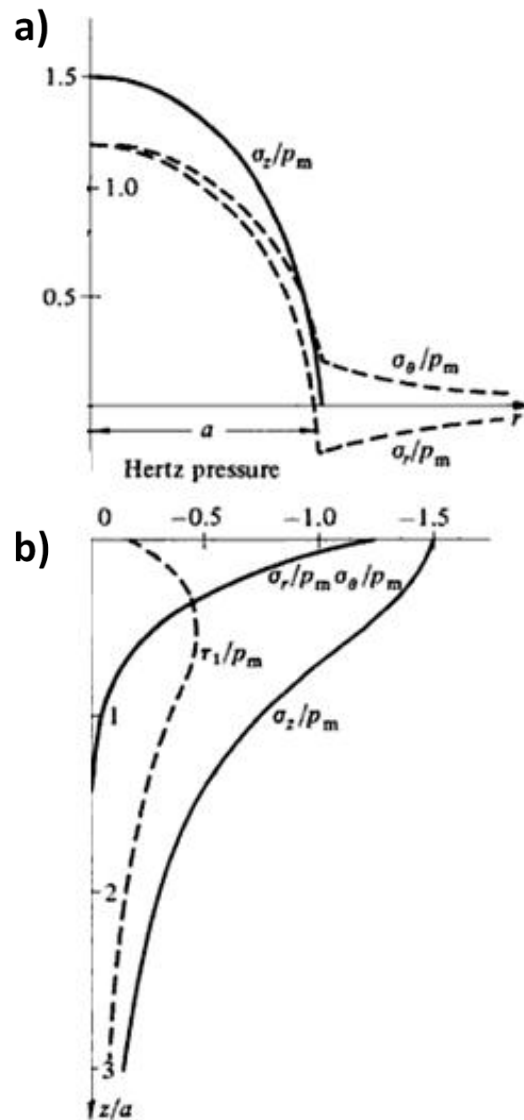


Figure 2-10: Stress Distributions (a) at the Surface and (b) along the Axis of Symmetry Caused by Hertz Pressure for a Poisson Ratio of 0.3 [Johnson, 1985].

As shown in Figure 2-10a, the researcher found that at the contact surface, the stress components are all compressive except outside the loaded circle where the radial stress (σ_r) is tensile. This is where the greatest tensile stress occurred, which related to the ring cracks observed during indentation tests of brittle materials. Stresses beneath the surface along the centre axis are

shown in Figure 2-10(b). They found that the maximum principal shear stress in the field (τ_1) occurs at a depth of approximately half of the contact radius. As a result, plastic yielding would be expected to initiate beneath the contact surface [Johnson, 1985].

However, when the response of the solid material is elastic-plastic, Hertzian theory is limited due to the assumptions stated earlier. Therefore, elastic-plastic contact modelling was performed both by an analytical method and by a finite element method in order to capture the plastic deformation behaviour of the solid material.

Marsh [1964] and Johnson [1970] used an analytical approach and obtained the plastic zone formation of an elastic-perfectly plastic indentation, based on the observations that the subsurface displacement produced by an indenter is approximately radial from the first contact point, with roughly hemispherical contours of equal strain. Later work done by Tabor [Tabor, 1986] suggested that the first yield for a spherical contact occurs when the mean pressure (p_m), approximately equals to 1.1 times of the yield stress (Y) of softer material ($p_m \sim 1.1Y$). As the load on the indenter increases, the mean pressure increases till it reaches approximately 2.8 times the yield stress ($p_m \sim 2.8Y$), where fully plasticity is reached.

The finite element method has also being widely used for the simulation of a spherical contact. One of the earliest studies by the finite element method of two dimensional stresses beneath a cylindrical indenter was made by Akyuz and

Merwin [1968]. More complete FEA simulations for indentation of an elastic plastic solid by a cylinder or sphere were performed by Hardy et al. [1971] and Lee et al. [1972]. Although they obtained the development of the plastic zone beneath the contact area for a range of different loading force, their models were restricted to elastic-perfectly plastic solid only. The influence of strain hardening and different elastic properties on contact pressure, surface and subsurface stress was presented by Kral et al. [1993] based on a rigid sphere on an elastic-plastic half-space model. He used commercial software ABAQUS to perform the simulations and assumed isotropic hardening in his analysis. During the plasticity analysis, the deformation gradient of the elastic-plastic half-space is decomposed into elastic and plastic parts. Von Mises yielding criterion is adopted in his study,

$$\sigma_M = \left[\frac{3}{2} S_{ij} S_{ij} \right]^{\frac{1}{2}} = \sqrt{\frac{(\sigma_{11}-\sigma_{22})^2 + (\sigma_{22}-\sigma_{33})^2 + (\sigma_{11}-\sigma_{33})^2 + 6(\sigma_{12}^2 + \sigma_{23}^2 + \sigma_{31}^2)}{2}} \quad (11)$$

where σ_M is the von Mises equivalent stress and S_{ij} is the deviatoric stress tensor. When the Von Mises equivalent stress, σ_M , is smaller than the initial yield stress, Y , the usual elastic constitutive equations apply. When $\sigma_M = Y$, the strain hardening relationship and flow rule applies. The isotropic strain hardening relationship is given by

$$\sigma^0 = K \varepsilon_{eq}^n \quad (12)$$

where σ^0 is the yield stress, K is the strength coefficient, n is the strain hardening exponent and ε_{eq} is the equivalent plastic strain.

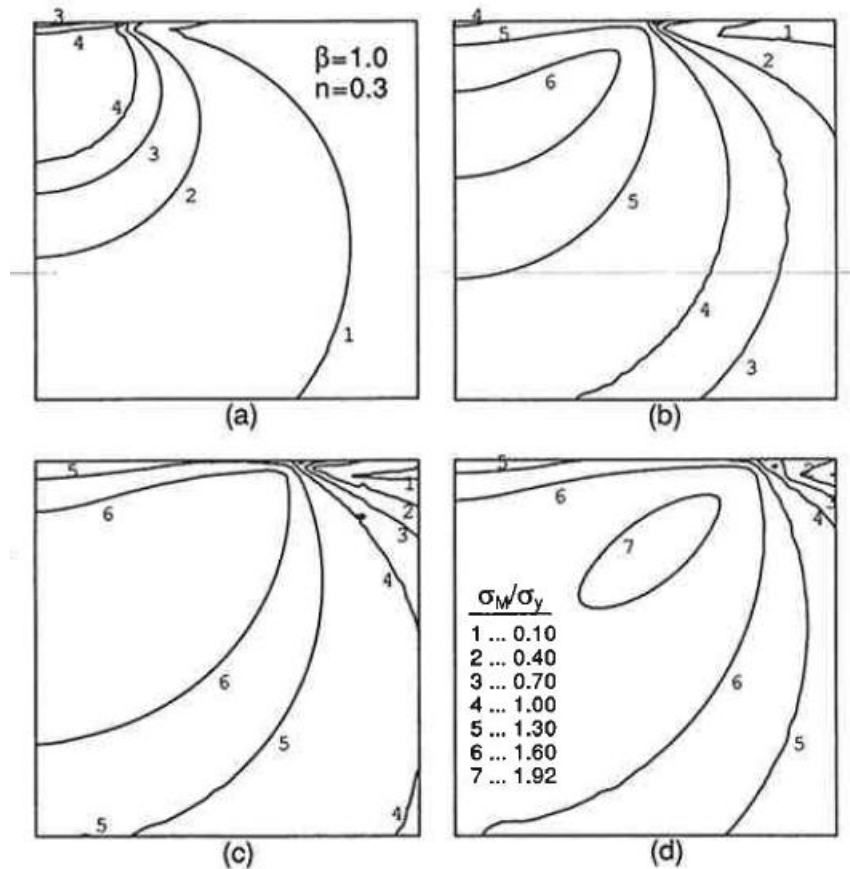


Figure 2-11: Contours of von Mises Equivalent Stress for Loads P/P_Y Equal to (a) 15.5, (b) 100.6, (c) 200, and (d) 300. [Kral et al. 1993]

Figure 2-11 shows the von Mises equivalent stress in the half-space for an elastic plastic material at different load. Here, P_Y is the initial yield load. In Figure 2-11(a), at a load $P/P_Y=15.5$, the plastic zone is surrounded by the elastic zone and it almost reaches the surface of the contact. Then as the load increases, the elastic zone diminished and eventually disappears in Figure 2-11 (b) (c) and (d). At the same time, the point of maximum von Mises stress moves radially outward from the center and toward the surface. This observation of initial plastic yielding was expected to initiate beneath the surface, as verified with the Johnson's

concept discussed earlier in this chapter. Thus, Karl was able to plot the stress distribution at different loads during the elastic-plastic spherical contact situation, which could be used for the FEA indentation modelling of the MMRI tribometer.

However, Karl's indentation model did not include friction in his model. Later work done by Taljat and Pharr [2004] took the friction into consideration and concluded that the contact friction affects the pile-up geometry. They found that friction affects pile-up in a manner that depends on the strain hardening exponent, n , as shown in Figure 2-12. When $n=0$, friction reduces the amount of pile-up significantly. When $n=0.5$, sink-in predominates the indentation profile and friction effects are negligible.

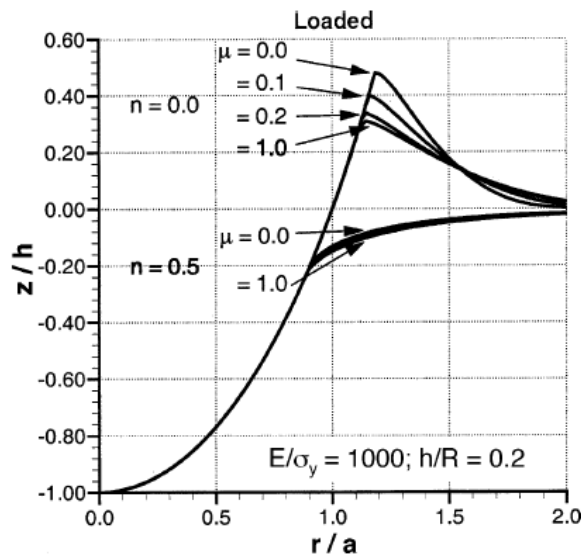


Figure 2-12: Effect of Contact Friction on the Indentation Profile: r -radial distance; a -contact diameter; z -vertical distance; h -indentation depth [Tajjat & Pharr, 2004].

2.3.2 Sliding contact

Most numerical studies of tribological contact focused on the linear tangential loading and sliding of either the indenter or the workpiece. Typical elastic sliding contact system is shown in Figure 2-13.

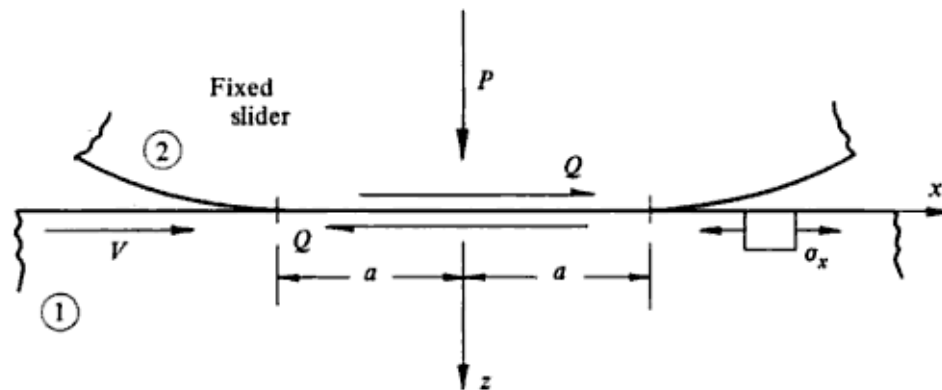


Figure 2-13: Schematic of Two Solids in a Sliding Contact [Bhushan, 1996]

The slider, carrying a normal load P , moves from right to left over the fixed flat surface in a direction chosen parallel to the x -axis. Neglecting the friction effects, the size of the contact area and the pressure distribution could be obtained using the Hertzian theory discussed earlier. Then assuming Amontons-Coulomb's law of friction, the tangential traction per unit area acting on the surface is given by:

$$q(x) = \mp \frac{3\mu P}{2\pi a^2} (a^2 - x^2)^{1/2} \quad (13)$$

where the negative sign is associated with a positive direction of the motion. Then based on this distribution equation, the stress components in the solid can be obtained by integrating throughout the contact area (Johnson, 1985).

Hamilton and Goodman [1966] used a different approach by extending a method introduced by Green [1949] for the stress analysis of a normally loaded solid with the friction effects. Figure 2-14 shows the normalized principal stress in the x-direction at the contact surface for a different coefficient of friction. When $\mu=0$, the radial stress is tensile outside the contact surface similar to what was discussed earlier in elastic normal contact. As the friction coefficient increase, the tangential force starts to add tension on the right side of the contact and subtract tension on the other side. As a result, depending on the surface friction, there will be compressive stresses along the x-axis at the leading edge of the contact and a maximum tensile stress at the trailing edge. Their results were later verified, analytically by King [King & O’Sullian, 1987] and Nowell [Nowell & Hill, 1988], and experimentally by J. Scheibert [2009].

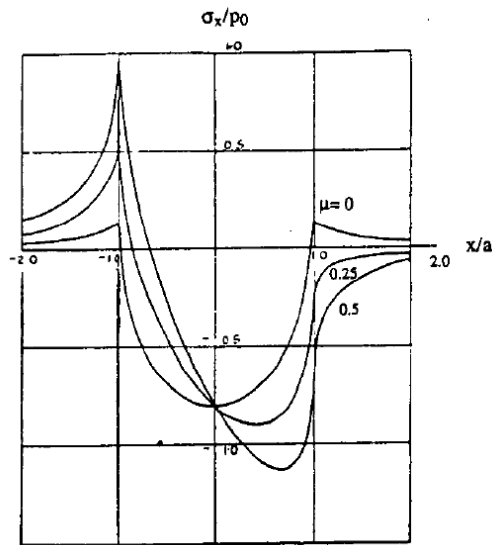


Figure 2-14: Normalized Stress σ_x/p_0 along the x-axis at the Contact Surface for Different Coefficient of Friction for an Elastic Contact. [Hamilton & Goodman, 1966]

Analytical calculations done by Johnson and Jefferies [1963] used von Mises yield criteria to determine the location of the initial yield in a sliding contact. It has been found that the tangential force will bring the point of maximum shear stress towards the surface as the coefficient of friction is increased. Thus, they found that yielding initiates in the subsurface region when the friction coefficient μ is small (<0.3), and at the contact surface when the friction coefficient exceeds 0.3. Later Work done using finite element modeling by Djabella [Djabella & Arnell, 1993] and Tian [Tian & Saka, 1991] shows similar trends of friction effects on sliding contacts. A fully 3-D model for an elastic sphere sliding over an elastic-plastic workpiece was subsequently developed by Kral and Komvopoulos [1996]. They found that increasing friction will cause a slight decrease in groove depth with sliding distance. They also found that higher friction will cause larger front and transverse pile-up, which indicate that increasing the coefficient of friction will produce more deformation of the surface material in the sliding direction. More comprehensive simulations were later performed by Ye [Ye & Komvopoulos, 2003] and Holmberg [2004]. They both found that high friction loading promotes plasticity and intensifies the von Mises and first principal stresses in the trailing part of the contact area, which causing cracks to occur.

Based on the finite element normal and linear sliding contact modelling technique reviewed in this section, a model involving indentation and fixed axis rotational sliding contact will be the main focus of this research. Temperature effects at the contact interface will also be examined.

Chapter 3. System Configuration

3.1 MMRI Tribometer

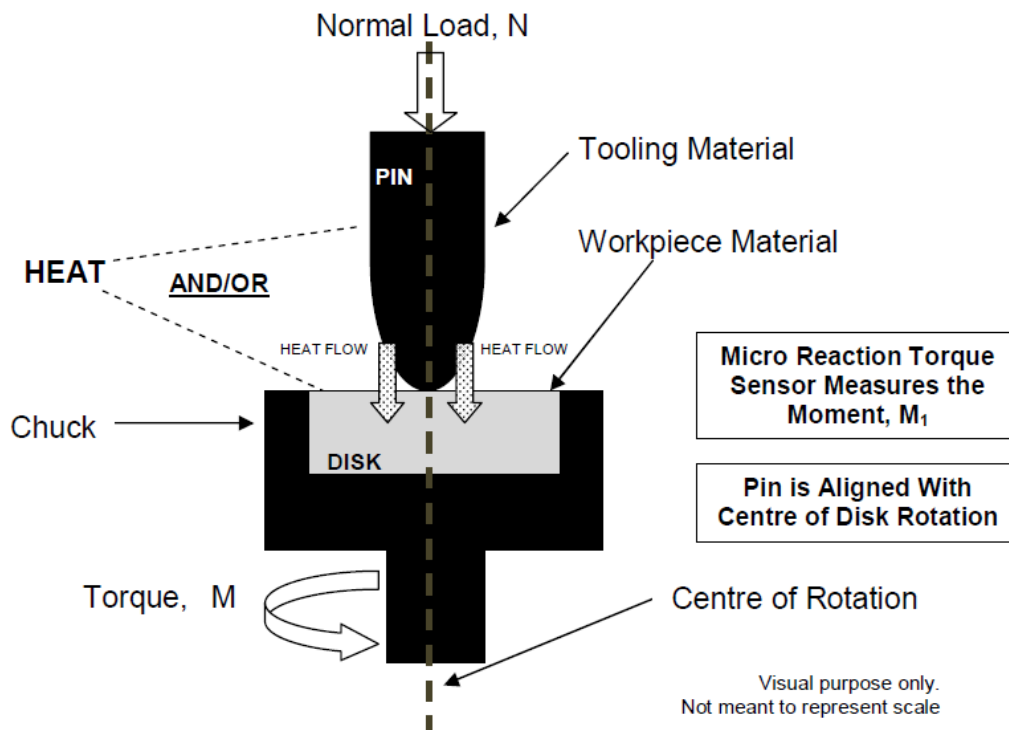


Figure 3-1: Illustration of the MMRI Tribometer [Andrew, 2010].

The MMRI tribometer shown in Figure 3-1 is constructed as a modified Brinell hardness test setup by Biksa in order to simulate the subsurface plastic flow under high temperature and near seizure conditions. The spherical tipped pin made of tooling material is loaded under high stress and high temperature against a flat disk made of the workpiece material. Then based on the output parameters obtained from the MMRI tribometer, a coefficient of friction could be calculated and used as a preliminary screening parameter for selecting tool coatings.

3.2 Pin & Disk

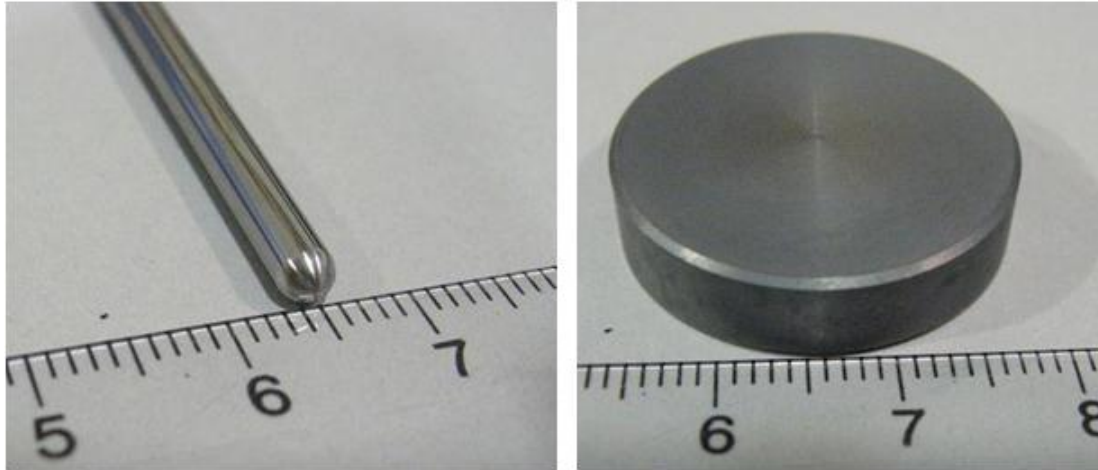


Figure 3-2: Pin and Disk (All dimensions are in mm).

The pin used for the tribometer setup is a hemispherical pin similarly to the Brinell hardness test. It is made of tungsten carbide with 6% cobalt and has 92.5 Rockwell C hardness. The diameter of the pin is 3mm so that when 2000N force is applied on the pin, the Titanium alloy workpiece could achieve full plastic deformation.

The disk is made of Ti6Al4V with 37 Rockwell hardness. It is designed to be a minimum of around 5mm thick and in 10mm diameter in order to allow the load and the torque to be insignificant at the boundaries.

3.3 Testing Procedure

Preparation work including calibration and cleaning needed to be performed before the testing. The pin is aligned such that it is on the axis of rotation of the disk. The system was firstly loaded to 1000N and held for 1 minute to ensure that the workpiece material is plastically deformed. Then data acquisition system is turned on and the heat is applied to the pin. Once the desired temperature is reached, the pin was loaded to 2000N. Then, with the constant temperature and normal load still applied, the disk is rotated relative to the pin at 1 revolution per minute for 10 seconds. All the variables including force, temperature and torque were stored during the test. The indentation diameter of the disk could be measured under the microscope after the test. Based on the output parameters generated during the experiment, the coefficient of friction between the pin and disk at different temperatures could be calculated using the equation (3).

Chapter 4. Numerical Model

4.1 Material Constitution Model

Due to the temperature effect of this model, Johnson-Cook material model is selected. This model has been widely used for describing the plastic material behaviour at high strain rates and high temperatures. The flow stress can be expressed as:

$$\sigma = (A + B\varepsilon^n) \left[1 - \left(\frac{T - T_r}{T_m - T_r} \right)^m \right] \left(1 + C \ln \frac{\dot{\varepsilon}}{\dot{\varepsilon}_0} \right) \quad (14)$$

where σ is the material flow stress, ε is the equivalent plastic strain, $\dot{\varepsilon}$ is the strain rate, $\dot{\varepsilon}_0$ is the reference strain rate, T is the temperature of the material, T_r is the room temperature and T_m is the melting temperature. The five empirical constants are as follows: A is the initial yield stress, B is the hardening modulus, n is the work-hardening exponent, C is the strain rate dependency coefficient and m is the thermal softening exponent. The first parenthesis is an elastic-plastic term which shows strain hardening of the material. The second parenthesis is the temperature softening term describing the temperature effects on flow stress. The last one is the viscosity term which represents the strain rate effect.

Table 4-1: Johnson-Cook Parameters for Ti6Al4V [Songwon et al., 2005]

A(MPa)	B(MPa)	n	m	T_r (°C)	T_m (°C)
997.9	653.1	0.45	0.7	25	1668

The material constants for the Johnson-Cook material model for Ti-6Al-4V alloy are given in Table 4-1 and mechanical properties are given in Table 4-2. Since we would like to model the plastic adhesive mechanism in near seizure conditions, which means that the rotational speed is very low, therefore, the strain rate dependency coefficient (C) is assumed to be zero in the equation, and only the elastic-plastic term and the temperature softening term will be considered for the FEA simulations.

Table 4-2: Mechanical Properties of Ti6Al4V

Modulus of Elasticity (MPa)	113,800
Poisson's Ratio	0.343
Thermal Conductivity (W/m.K)	7.2
Mean coefficient of Thermal Expansion 0-800°C	9.9×10^{-6}

4.2 Friction Models

Friction is modeled using a standard Coulomb's friction model. It relates the maximum allowable frictional shear stress across an interface to the contact pressure between the contacting bodies. The equation to calculate this critical shear stress is $\tau_{crit}=\mu p$, where p is the contact pressure and μ is the coefficient of friction. The friction model assumes that μ is the same in all directions. For a three-dimensional simulation there are two orthogonal components of frictional shear stress, τ_1 and τ_2 , along the interface between the two contact bodies. The two shear stress components are combined into an "equivalent shear stress", τ_{eq} , for the stick/slip calculations, where $\tau_{eq}=\sqrt{\tau_1^2 + \tau_2^2}$.

If the equivalent shear stress, τ_{eq} , is less than the critical shear stress, τ_{crit} , then no relative motion occurs. This concept could also be shown in Figure 4-1. When the equivalent shear stress between two bodies is lower than the contact pressure multiplied by a constant COF ($\tau_{eq}<\mu p$), the two bodies will stick, and sliding of the surface will only occur when $\tau_{eq}\geq \mu p$.

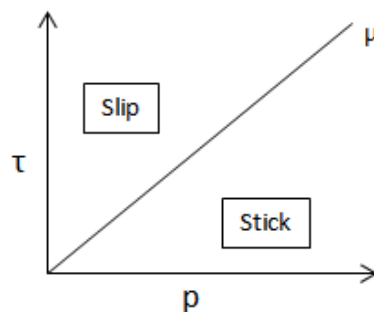


Figure 4-1: Stick and Slip Regions for Coulomb's Friction

4.3 Contact Algorithm

Understanding the contact algorithm used in ABAQUS is very important. In ABAQUS, there are two approaches to track the relative motion of two interacting surfaces in mechanical contact simulations. The first approach is the “finite sliding” formulation, which allows any arbitrary separation, sliding, and rotation between the contact surfaces. The second one is the “small sliding” formulation, which assumes that two bodies could undergo large motions, but there is relatively little sliding of one surface along the other. In other words, it assumes that the plane where the slave nodes may slide are never updated after the first increment, which means that a slave node will interact with the same local area of the master surface throughout the analysis. Therefore, although this formulation is computationally less expensive than the “finite sliding” formulation due to the reason above, it does not allow free sliding motion to occur at the contact surface. Since the relative sliding motion between the pin and disk need to be simulated in our work, the “finite sliding” formulation approach is selected for FEA simulation.

In order to simulate contact conditions, ABAQUS also needs to apply constraints at different locations on the interacting surfaces, and the locations and conditions of these constraints depend on the contact discretization in the overall contact formulation. One of the contact discretization used in ABAQUS is the “node to surface” contact, which each slave node on the slave surface interacts with a point of projection on the master surface on the master contact surface.

The other contact discretization is the “surface to surface” contact, which the approximate average location of the nearby slave nodes interacts with the master surface rather than an individual slave node itself. This means that the contact constraint will not only consider one slave node when interacting with master surface, but also consider the adjacent slave nodes. Thus, the fewer amounts of penetrations of master nodes into the slave surface will occur for this discretization as compared with the node to surface contact. Also, due to the fact that ABAQUS will try to resist the penetrations, forces will tend to concentrate at these nodes, which lead to non-uniform stress distribution across the surface as shown in Figure 4-2(a). On the other hand, “surface to surface” contact resists penetrations in an average sense over the nearby node regions, which will result a more smoothing stress distribution across the surface as shown in Figure 4-2(b). Therefore, the “surface to surface” contact discretization is used for our FEA simulation.

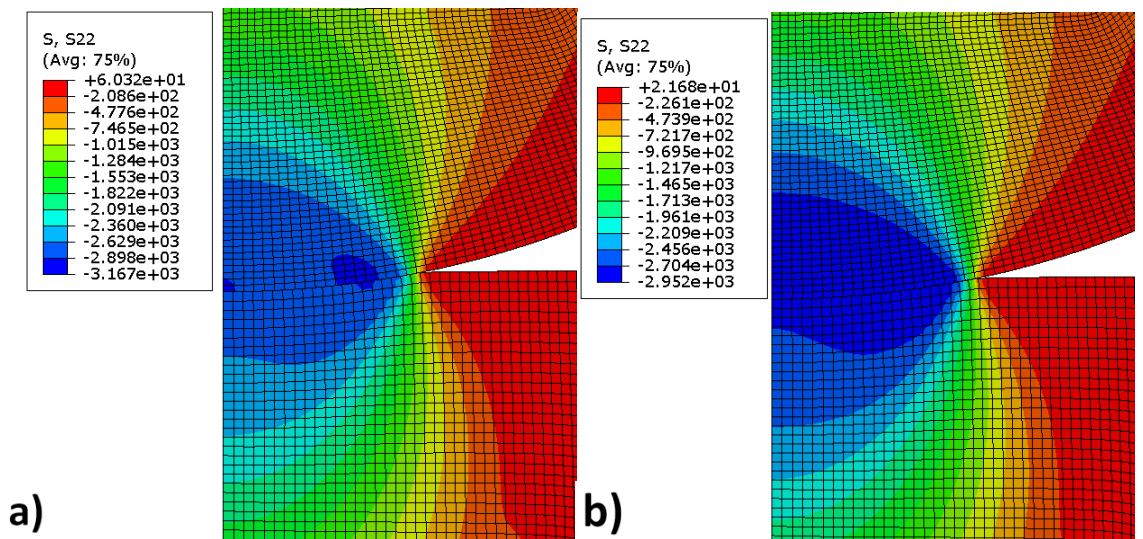


Figure 4-2: Normal Stress Distribution Obtained by Using (a) Node to Surface, (b) Surface to Surface Contact Algorithm.

4.4 FEA modeling

All the finite element tribometer models in this research were simulated using general FE code ABAQUS/Standard version 6.9-1. A 2D tribometer model was built initially to capture the stress distribution after the indentation process, and then a 3D model was built in order to include the rotation and heating processes.

4.4.1 2D modelling of indentation

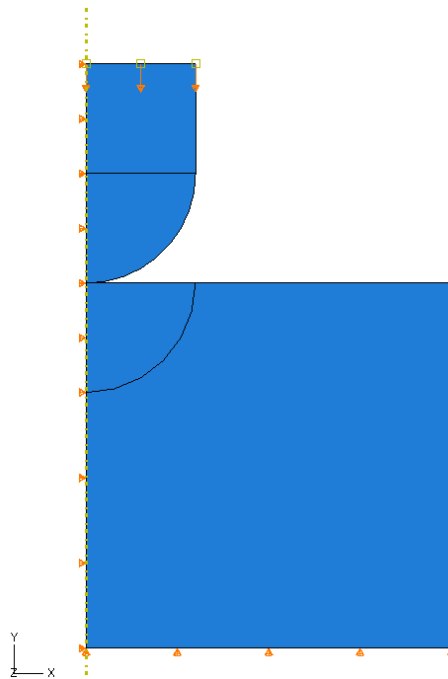


Figure 4-3: 2D Model of the Tribometer

Based on the tribometer setup in the MMRI, the pin is modeled to be 3mm in diameter. The disk is 5mm in radius and 5 mm thick, which is large enough to allow the stresses and the displacements to be insignificant at the boundaries. As

shown in Figure 4-3, the 2D axisymmetric model space was employed using a cylindrical coordinate system, with radial coordinate, x , and axial coordinate y . Due to the axisymmetric geometry, only half of the tribometer was considered. The mid-plane of the model was restricted to move only along the y -direction. The displacements at the bottom plane were assumed to be zero in the vertical direction. The required load or displacement is applied at the top surface of the pin.

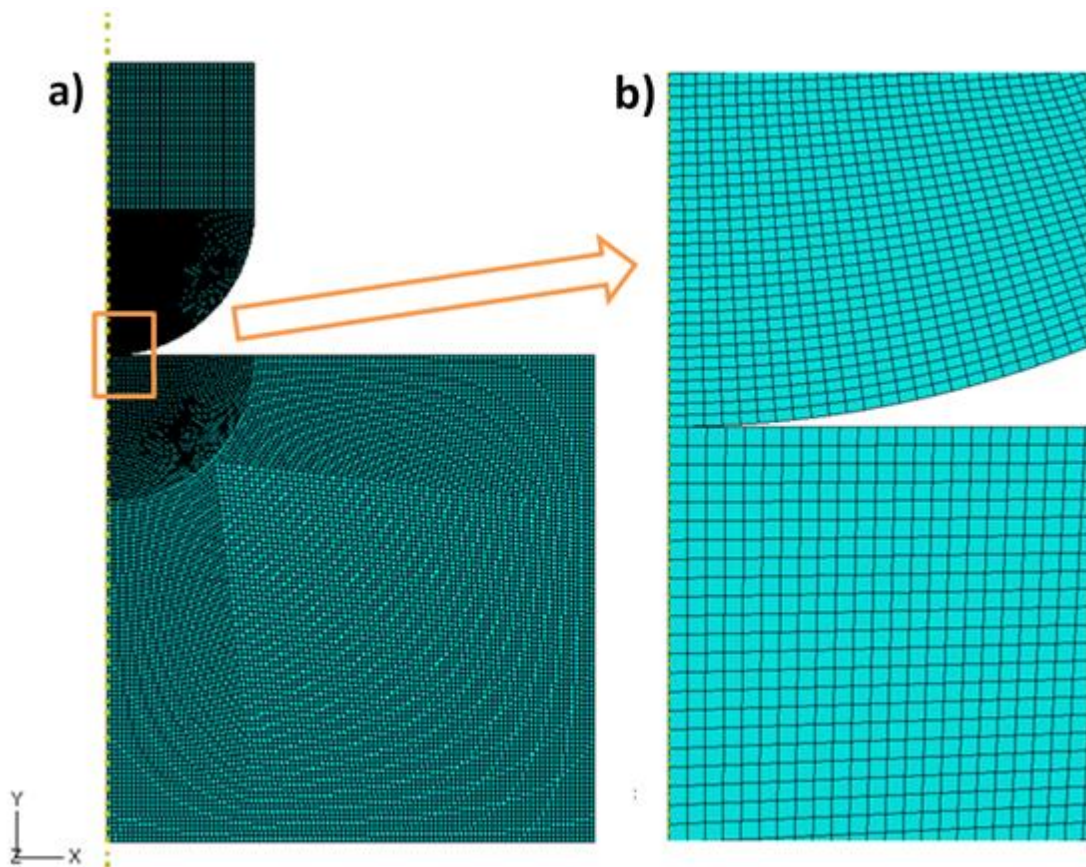


Figure 4-4: a) Overall Mesh; b) Mesh Details near the Contact Zone.

Figure 4-4(a) shows the overall finite element mesh and Figure 4-4(b) gives details of the mesh near the contact zone. The whole mesh is an

arrangement of 18649 CAX4R elements, and the total number of nodes are 19037. A total of 11860 elements are in the disk, and the remainder are in the pin.

In order to verify the modeling assumption and the finite elements mesh for this model, the FE results of elastic response are compared with the analytical solutions of the Hertzian contact theory. The FE results of the contact area are firstly compared with the analytical solutions of the Hertzian contact theory. According to Hertzian contact relation, the radius of contact area could be calculated as:

$$a^3 = \frac{4}{3} \frac{kPR}{E} \quad (13)$$

where a is the radius of the contact area, P is the indenter load, R is the radius of the indenter, and k is an elastic mismatch parameter, which is given by:

$$k = \frac{9}{16} \left((1 - \nu^2) + \frac{E}{E'} (1 - \nu'^2) \right) \quad (14)$$

In the above equation, E and ν are the Young's modulus and Poisson's ratio of the indenter and specimen respectively, and E' and ν' are the corresponding values for the indenter.

In Figure 4-5, the analytical solutions of the indentation radius is compared with the finite element solutions at different applied load. The discrepancy between the FE results and the corresponding analytical solutions was found to be negligible.

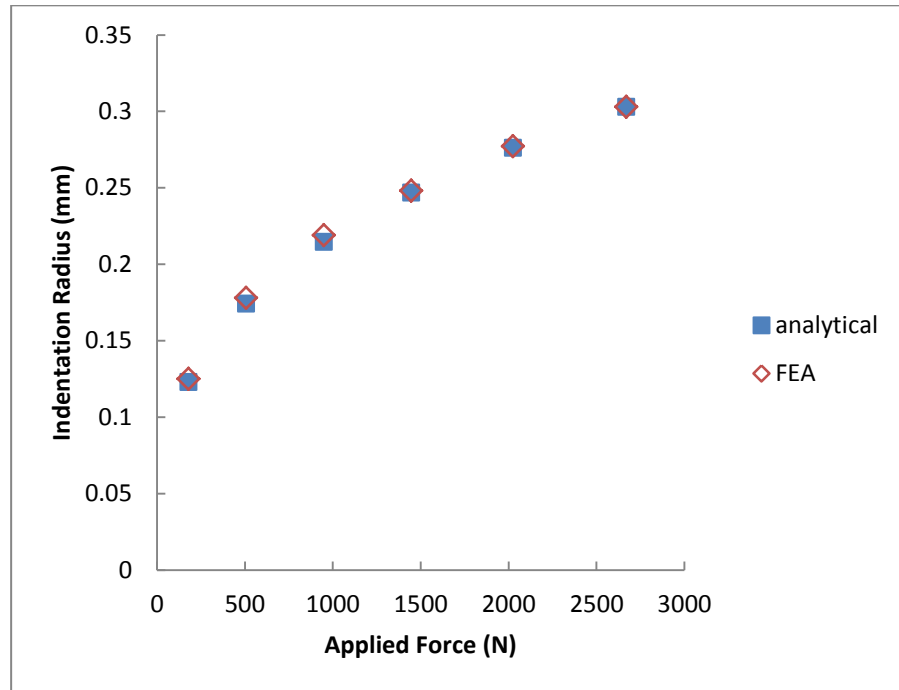


Figure 4-5: Comparison of Contact Area.

The FE results of the normal stress field were also compared with the analytical solutions of the Hertzian stress field. According to the Hertzian stress distribution equation, the normalized normal pressure distribution within the interior of the specimen is:

$$\frac{\sigma_y}{p_m} = -\frac{3}{2} \left(\frac{z}{u^{1/2}} \right)^3 \frac{a^2 u}{u^2 + a^2 y^2}, \quad (15)$$

where:

$$u = \frac{1}{2} \{ (r^2 + y^2 - a^2) + [(r^2 + y^2 - a^2)^2 + 4a^2 y^2]^{1/2} \} \quad (16)$$

and the mean contact pressure is:

$$p_m = P / (\pi a^2) \quad (17)$$

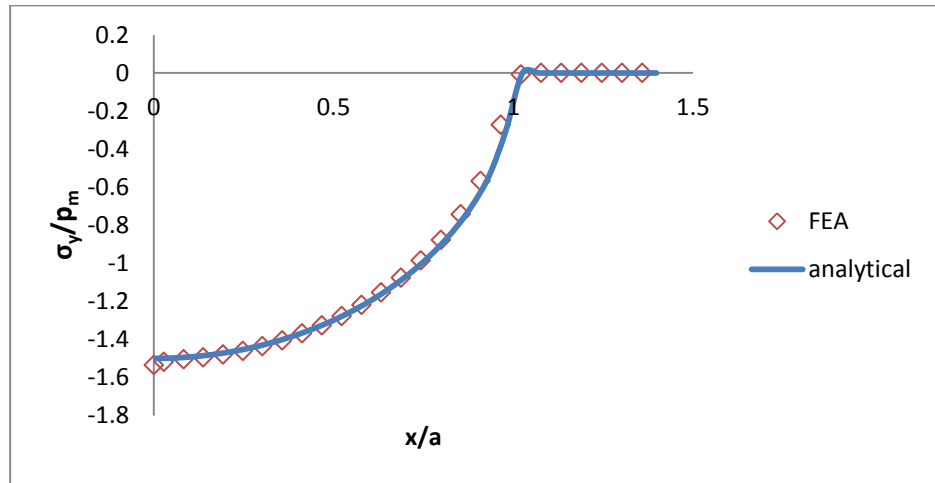


Figure 4-6: Comparison of the Normalized Normal Stress at the Contact Surface

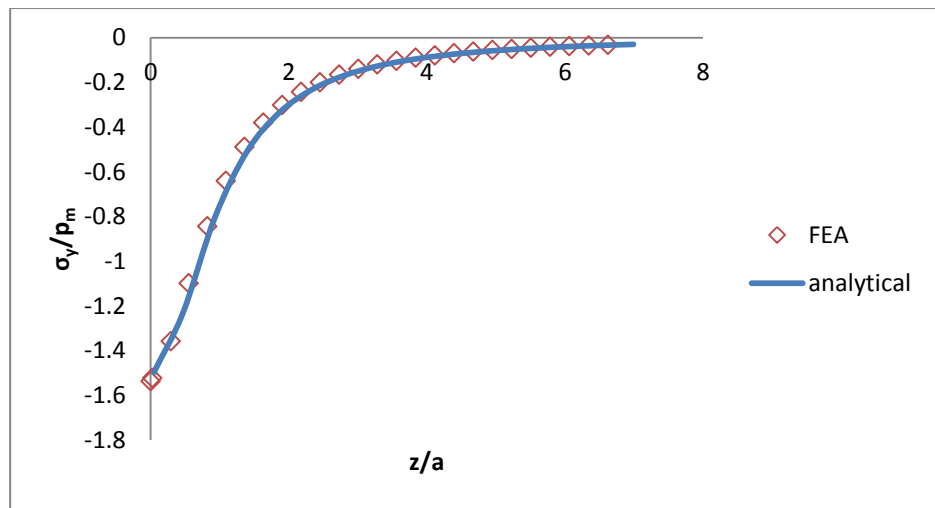


Figure 4-7: Comparison of the Normalized Normal Stress along the Axis of Symmetry.

For this finite element simulation, the contact radius, a , was about 0.2190mm. Stresses and coordinates were normalized by the mean contact pressure, p_m , and the contact radius, a , respectively. Figure 4-6 and Figure 4-7 show the normal stresses at the contact surface and along the axis of symmetry, respectively. It can be seen that there is fairly good agreement between the FE

results and analytical Hertzian results. The small errors could be attributed to the averaging of the stress data from integration points to boundary nodes and the discretization of the continuous surface. Therefore, it may be concluded that the finite element mesh and modeling assumptions are appropriate for simulating the indentation of a half-space by an elastic indenter.

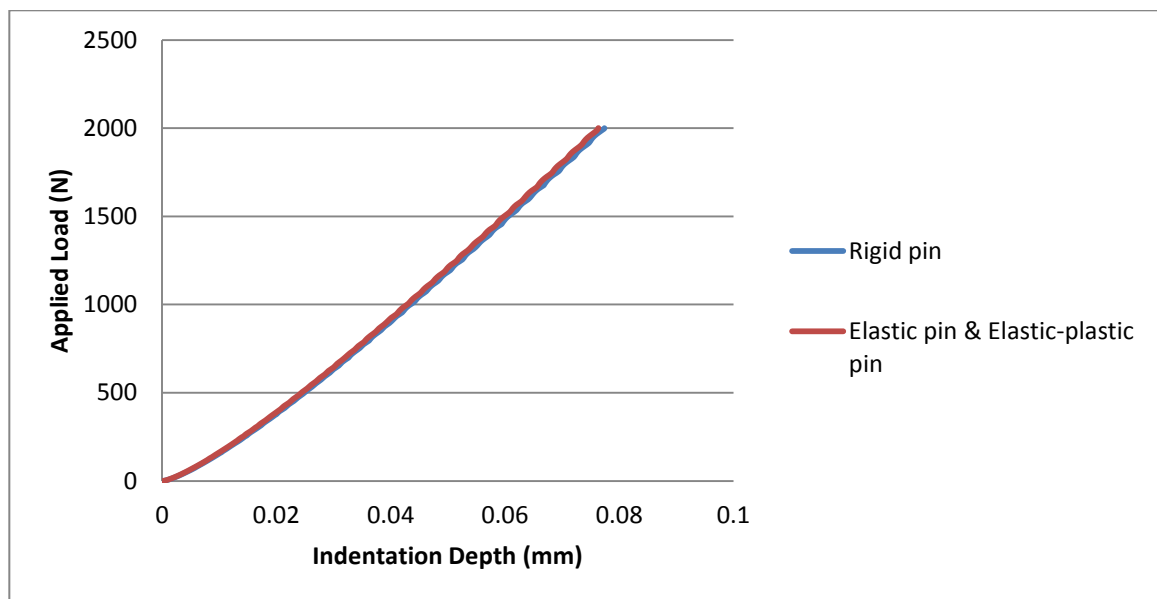


Figure 4-8: Comparison of the Load vs. Displacement Curve.

Due to the limitation of our computer's primary memory, it is very important to evaluate the possibility of using a rigid body for the pin, especially during 3D simulations. Therefore, simulations of indentation by using a rigid pin were compared with the ones using an elastic pin and elastic-plastic pin. Since the yield stress of the WC-6Co is extremely high, the yielding is expected to be never reached during any load of indentation for the pin. As shown in Figure 4-8, the load-displacement curve for the rigid pin indentation is very close to the one for the elastic pin indentation when 2000N vertical force is applied on the pin. Table

4-3 also showed even smaller differences of the maximum von Mises stress, maximum normal stress and contact diameter between the two assumptions for the pin. Note that using a rigid pin will result a slightly greater indentation depth, contact diameter and maximum stresses compared with using an elastic pin due to the incompressibility of the rigid body. In view of the comparisons with the two assumptions for the pin, it may be concluded that a rigid body could be considered for modelling the pin.

Table 4-3: Comparison of Maximum Stresses and Contact Radius.

	Rigid pin	Elastic & Elastic-plastic Pin
Maximum von Mises Stress (MPa)	1315	1302
Maximum Normal Stress (MPa)	3105	3073
Contact Diameter (mm)	0.9114	0.9104

4.4.2 3D modelling of indentation

In order to include the rotational effects of the pin, the tribometer setup was modeled in 3D system. As shown in Figure 4-9(a), the 3D model was built by using a cylindrical coordinate system, with radial coordinate, x , and axial coordinate z . Similar to the 2D model, the pin is 3mm in diameter, and the disk is 5mm in radius and 5mm thick. The bottom of the disk is constrained in the vertical direction, and a temperature boundary condition was applied at the contact interface between the pin and the disk. Since the rotation speed is very low, the heat generated by the material plastic deformation and friction between two contact surfaces are neglected. Also, since the yield stress for tungsten carbide is never reached, and the elastic deformation is relatively small as mentioned earlier in the 2D model, the pin is modeled as a rigid body to save computing time.

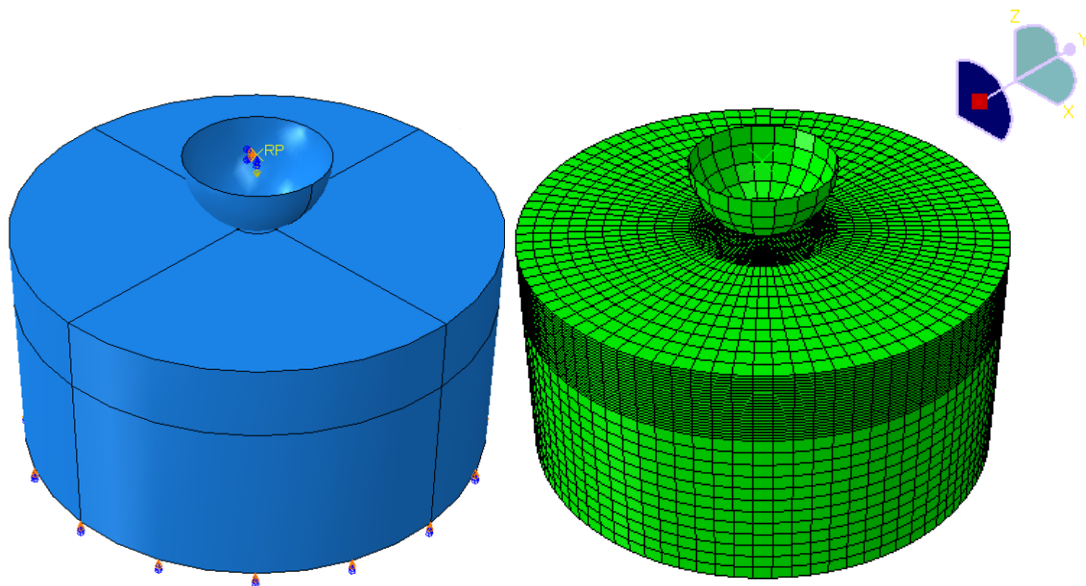


Figure 4-9: (a) 3D Model of the Tribometer; (b) 3D Overall Mesh.

Figure 4-9(b) shows the overall finite element mesh in 3D view. The whole mesh is composed of 102257 nodes and 97039 C3D8RT elements. The selection of the mesh size was a compromise between the solution accuracy and the computational cost. Since the stress gradient reached its highest value in the region directly underneath the rigid pin, a finer mesh is used near the rigid pin tip and a coarser mesh is used for other regions.

A Force-displacement curve for a 2000N indentation test for both the 2D and 3D simulations are compared in Figure 4-10. From the comparison of the results, it can be seen that there is fairly good agreement between the 2D and 3D modelling of the tribometer, which confirmed the validity of our 3D finite-element model and boundary conditions.

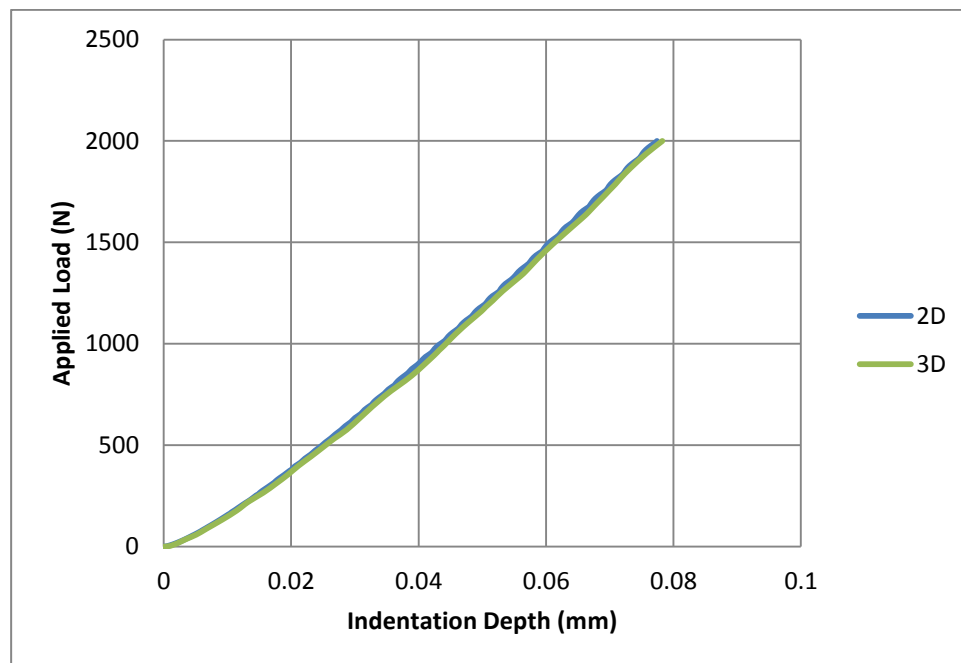


Figure 4-10: Comparison of Load Displacement Curve between 2D and 3D simulation.

Chapter 5. Results and Discussions

5.1 Comparison between FEA and MMRI experimental results

The FE results are compared with the experimental results for testing the accuracy of the FEA model. As stated earlier in Section 3.2, during MMRI experimental test, under a given interface temperature and a normal load, the torque moment and the indentation diameter could be measured, and thus, the MMRI COF could be calculated from Equation (3). However, for FEA simulations, the COF has to be an input parameter. Thus, under a given temperature and a normal load, the torque moment and indentation diameter could be obtained from FEA simulation. Both 2D and 3D FEA results will be compared with experimental results in this section.

5.1.1 2D simulation

The 2D FEA results are firstly compared with experimental results for checking the accuracy of the 2D FEA model. The pin is loaded with 250N, 500N, 1000N and 2000N force, and the indentation diameter for both the FEA simulation and experimental testing are measured and compared in Figure 5-1. It is shown that the FEA result of indentation diameter matches the experimental result well. However, the 2D FEA model does not capture the rotation effects of the pin, so the tribometer experimental output, torque, could not be compared

with FEA simulation at this stage. Therefore, the 2D FEA model is a reasonable representation of the indentation process of the MMRI tribometer.

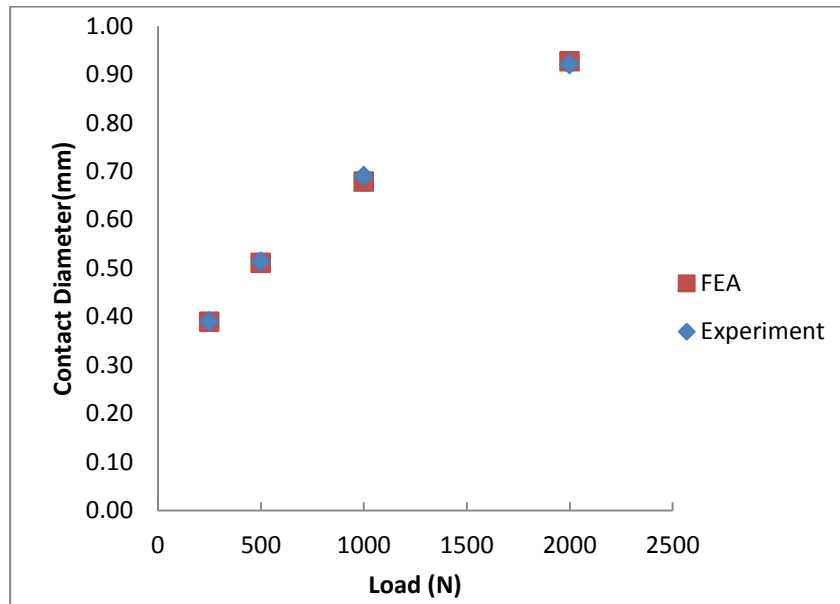


Figure 5-1: Contact Diameter under Different Loads for 2D Simulation.

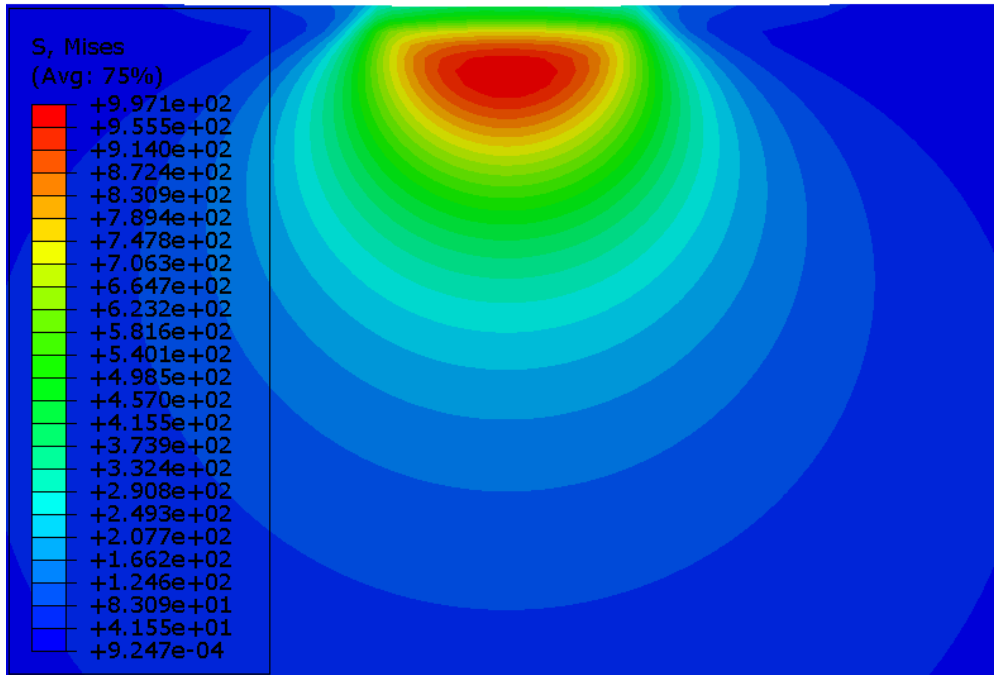
The trend of stress and strain distributions are also compared with the results from previous work discussed in Chapter 2. The evolution of the Von Mises stress distribution is plotted in Figure 5-2. Figure 5-2(a) shows the von Mises stress distribution under 4N normal force, where the onset of plasticity occurs ($Y=997.9\text{MPa}$). The maximum von Mises stress at this stage is found at the subsurface, some distance below the center of the contact region. This observation verifies the analysis of Hamilton and Goodman [1966], which shows the maximum principal shear stress occur beneath the surface. As the load increases, the region of maximum von Mises stress moves outward from the center towards the surface as shown in Figure 5-2(b), (c) and (d).

Similar observations are found for the equivalent plastic strain distribution in Figure 5-3. During initial contact, the surface is deformed elastically until the load reached around 4N, where the onset of plasticity occurs at the subsurface as shown in Figure 5-3(a). As the load increases, the plastic zone continues to grow until the edge of the plastic zone reaches the surface near the edge of the contact radius as shown in Figure 5-3(b). At this stage, however, there is no plastic deformation occurred at the contact surface below the pin. The region of maximum equivalent plastic strain is found on the axis of symmetry below the surface. When the load reaches about 375N, the contact surface is completely covered by the plastic zone as shown in Figure 5-3(c). This suggests that the normal load has to be at least 375N in order to achieve a complete plastic zone at the interface for experimental testing of the titanium alloy in MMRI. Both Figure 5-3(c) and (d) show that as the load increases, the maximum equivalent plastic strain moves radially away from the center towards the surface just inside the maximum contact radius. These observations of the von Mises stress distribution and the equivalent plastic strain distribution inside the disk are consistent with the results presented by Kral et al. [1993], which shows that as the load increases from elastic contact to plastic contact, the point of maximum von Mises stress and equivalent plastic strain moves outward from the center towards the surface.

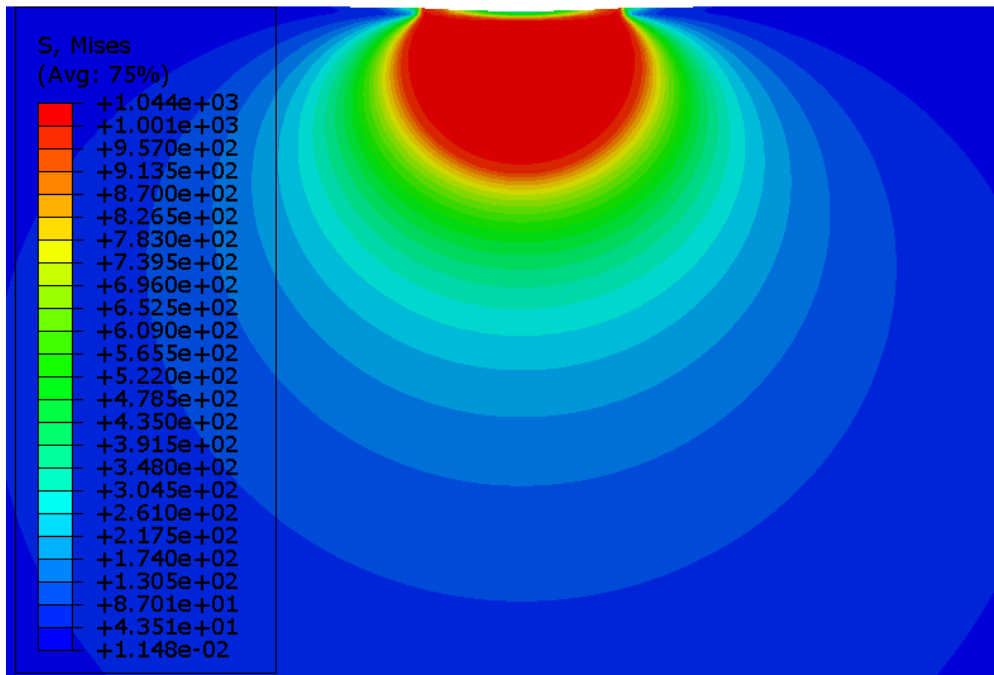
The Figure 5-4 shows the evolution of the normal stress distribution during the loading process. The normal stress distribution at the onset of plasticity is shown in Figure 5-4(a). The maximum normal stress found at the center of the

interface is about 1.651 GPa, and the mean normal stress after averaging the normal stress of surface contact nodes is 1.034GPa, which is about 1.04 times of the yield stress of the workpiece material ($Y=997$ MPa). This observation is in agreement with the work of Tabor [Tabor, 1986], which shows that the first yield for a spherical contact occurs when the contact stress approximately equal to 1.1 times of the yield stress (Y) of softer material. Figure 5-4(b), (c) and (d) shows that as the load increased, the normal stress distribution is flattened, with the maximum normal stress swifts toward the contact edge. These results are in agreement with previous indentation analyses performed by Komvopoulos, [1989] and Kral et al. [1993]. When the load reached 375N, the maximum normal stress is 2.745 GPa, and the mean normal stress after averaging the stress of surface contact nodes is approximately 2.65GPa. This result could be related to the Tabor's work discussed in Section 2.3.1. He found that the as the load on the indenter increase, the mean normal pressure increases till it reaches approximately 2.8 times of the yield stress, where fully plasticity is reached.

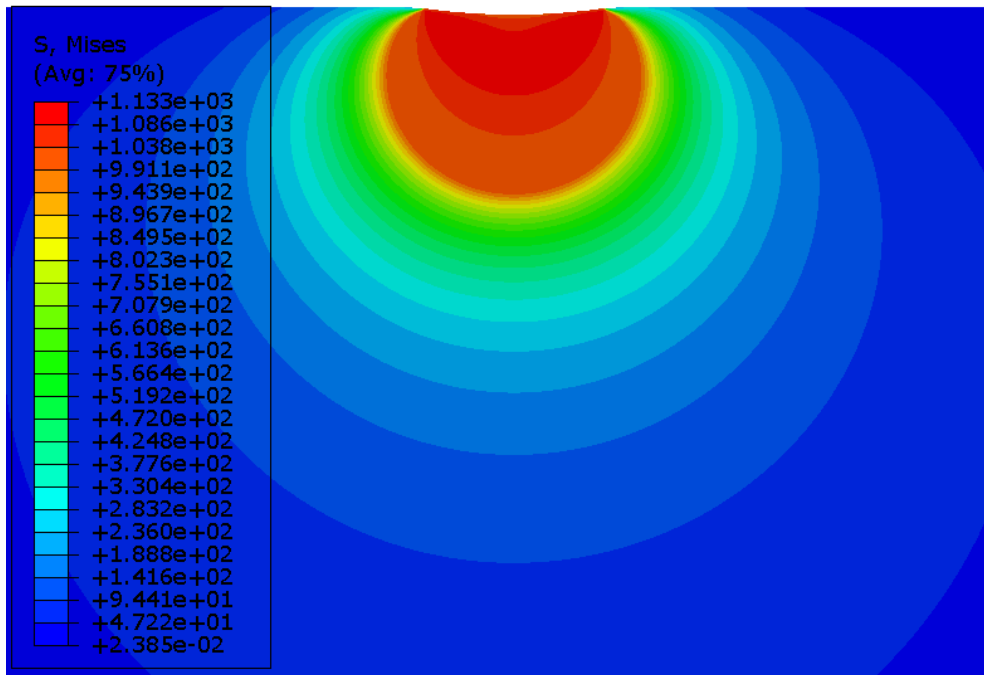
The contour of the orthogonal shear stress distribution is given in Figure 5-5. It is found that the shear stress is zero along the central axis and reached the maximum value at the area below the edge of the contact radius. As the load increases, the orthogonal shear stress is increased, which shows that this orthogonal shear stress is caused by indentation of the pin, not by the surface friction.



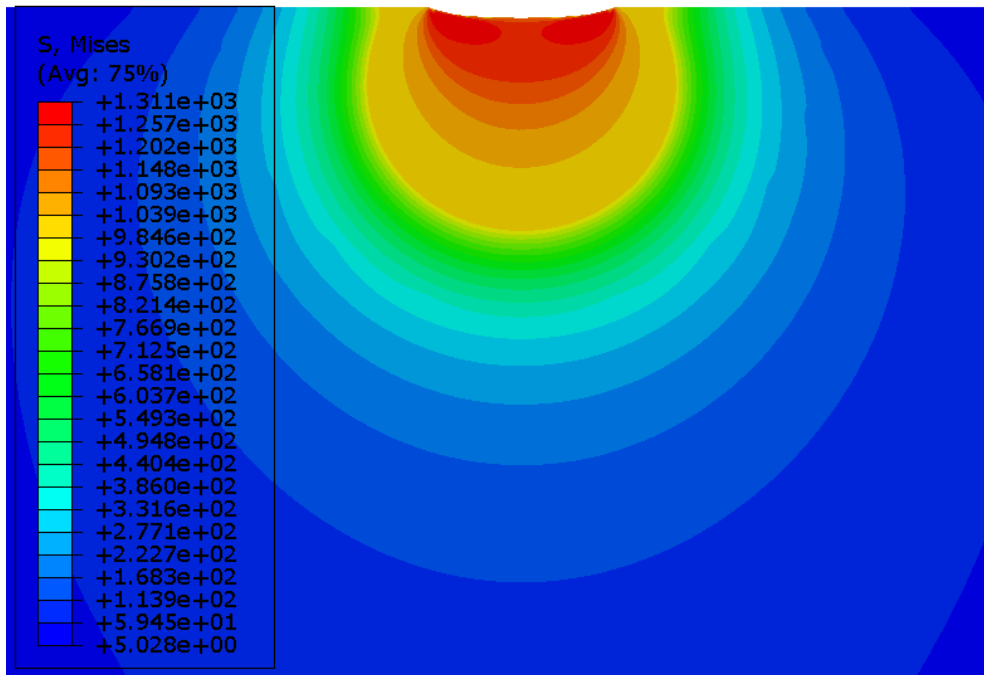
(a)



(b)

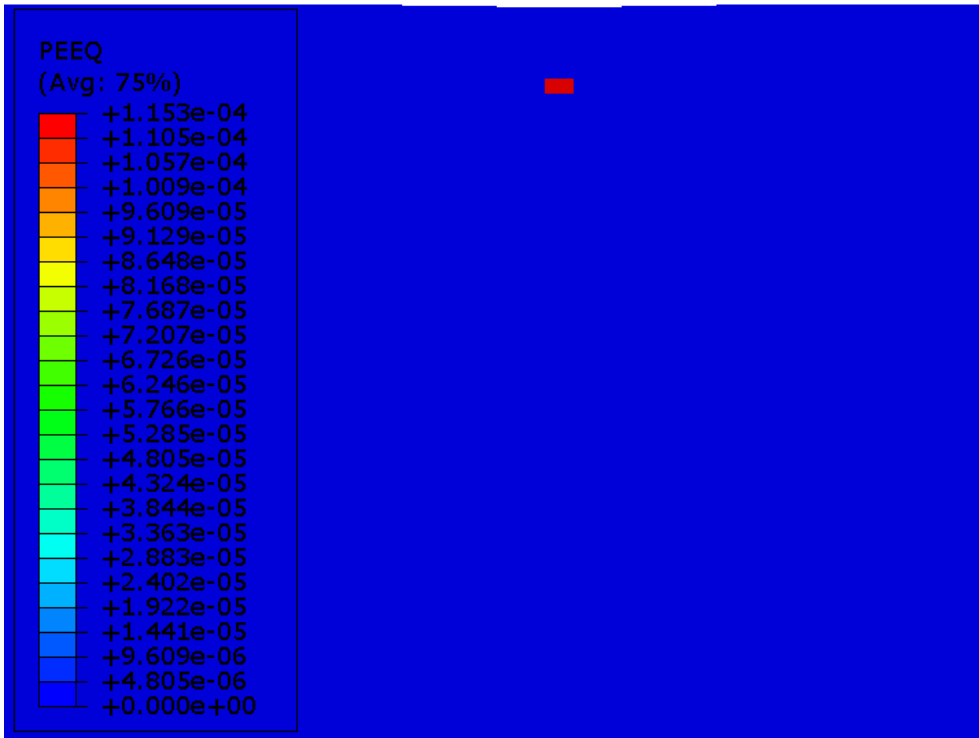


(c)

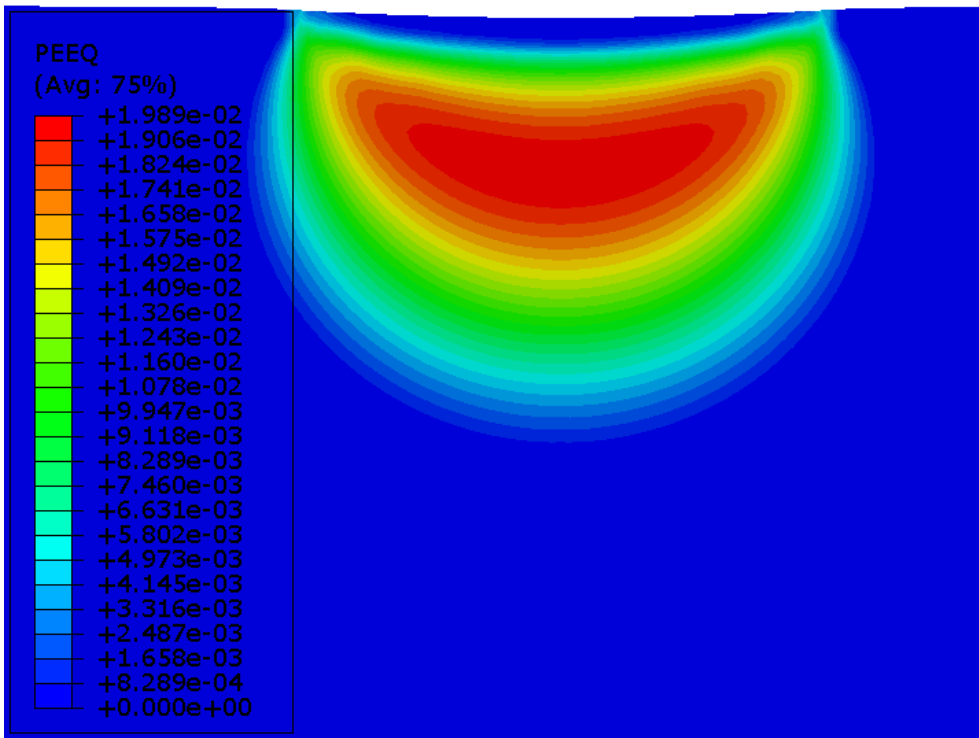


(d)

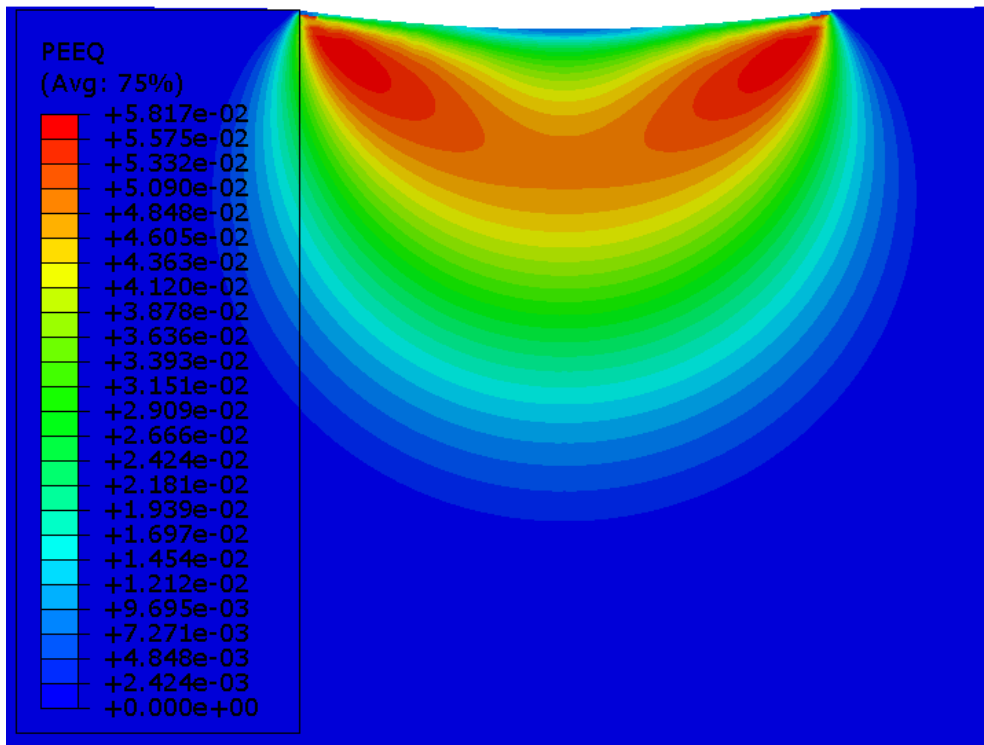
Figure 5-2: Contours of Von Mises Stress Distribution for Loads Equal to (a) 4N; (b) 56N; (c) 375N; (d) 2000N.



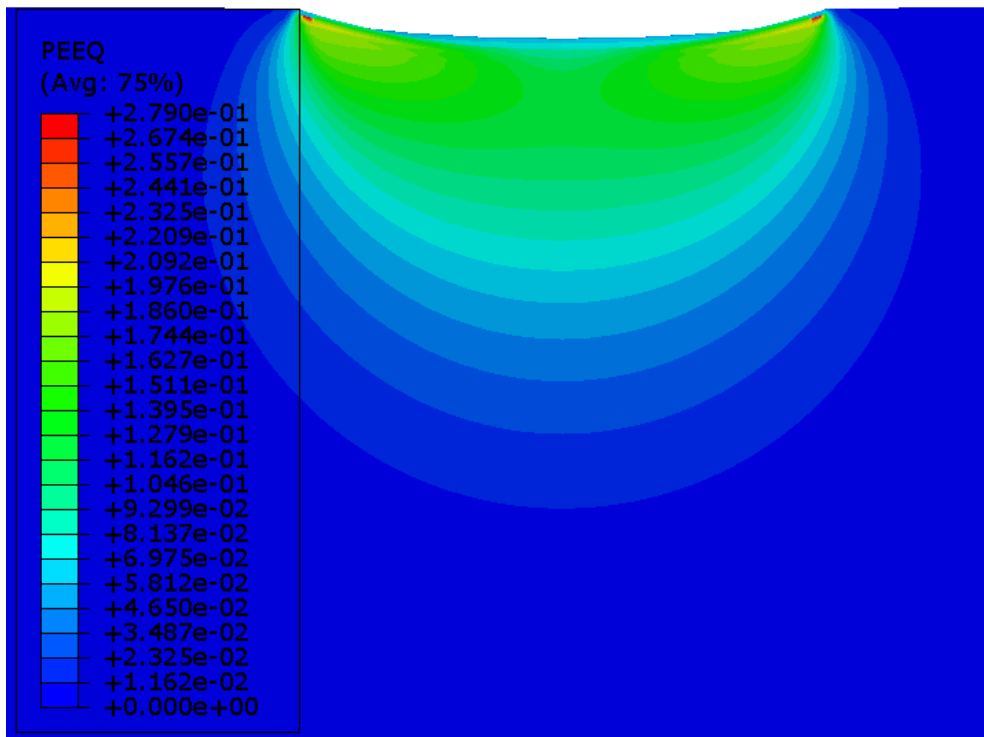
(a)



(b)

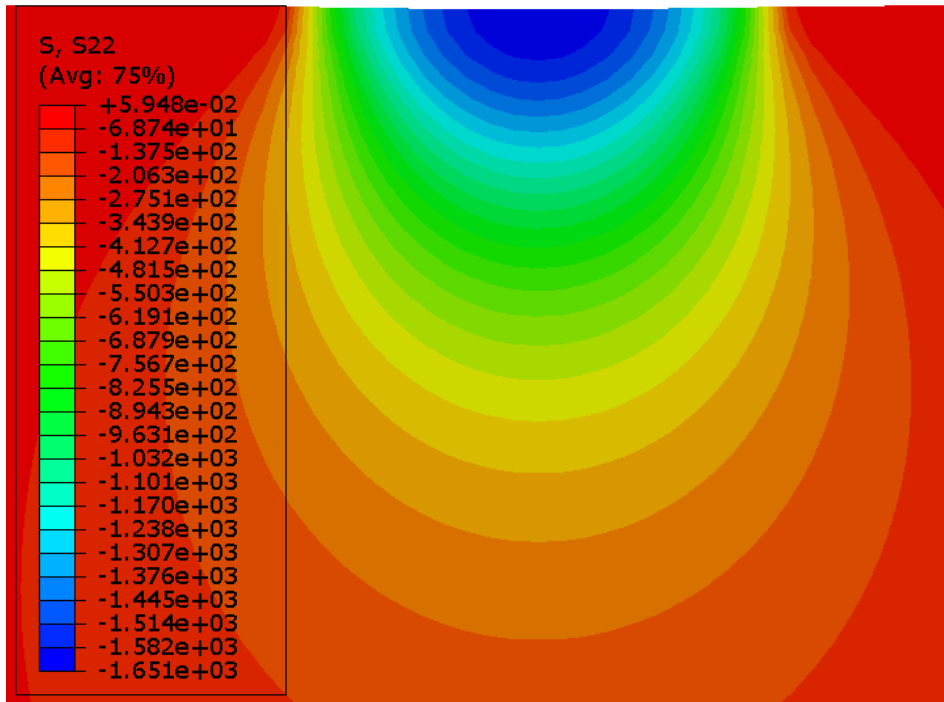


(c)

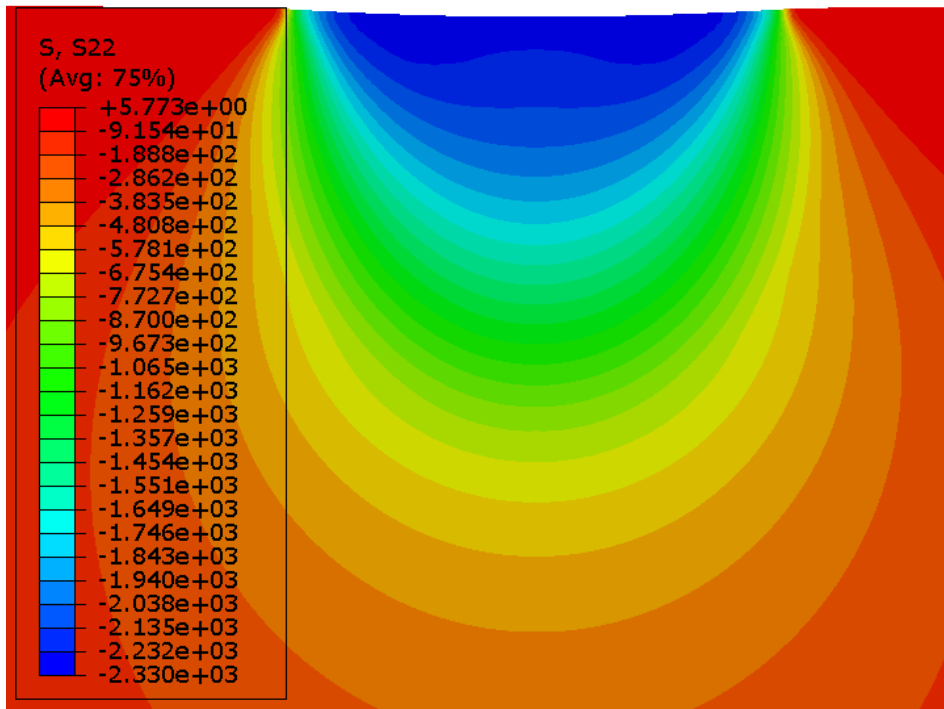
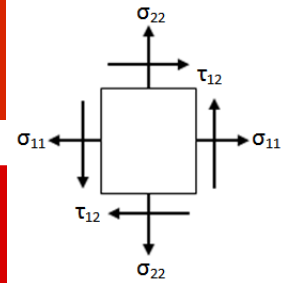


(d)

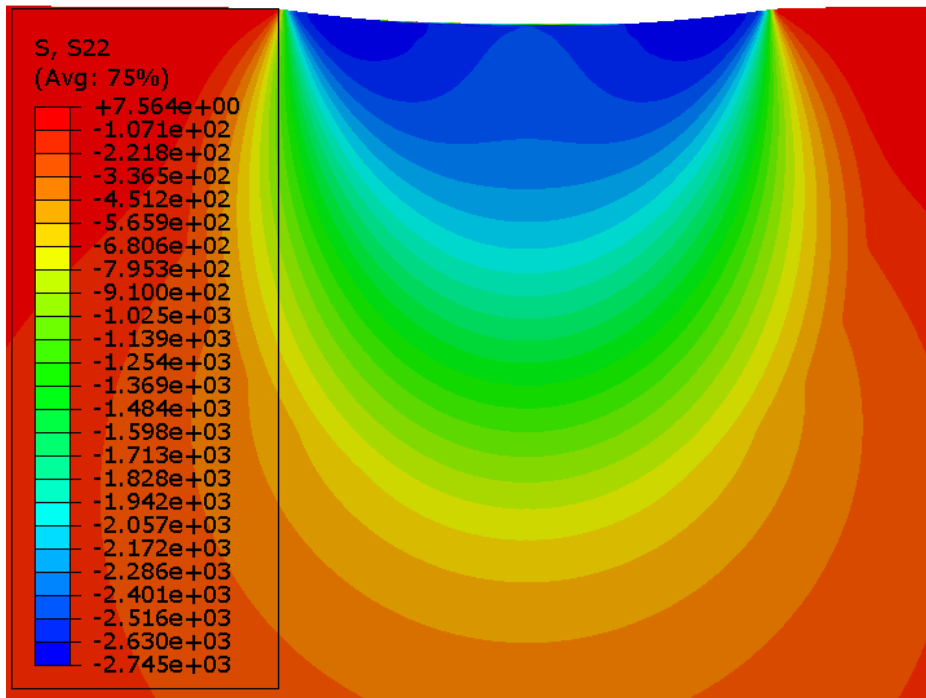
Figure 5-3: Contours of Equivalent Plastic Strain Distribution for Loads Equal to (a) 4N; (b) 56N; (c) 375N; (d) 2000N.



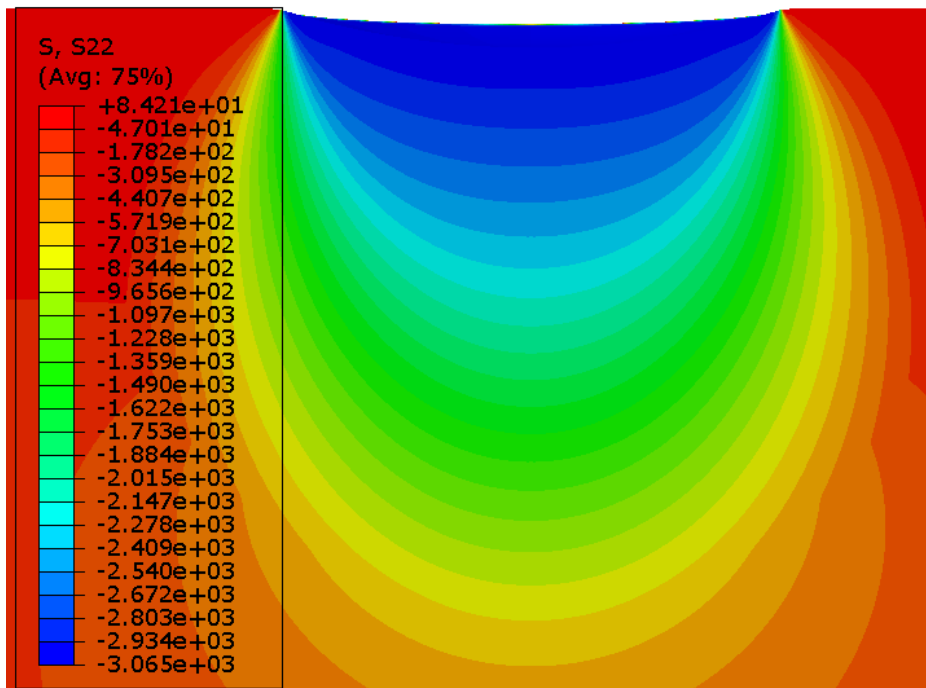
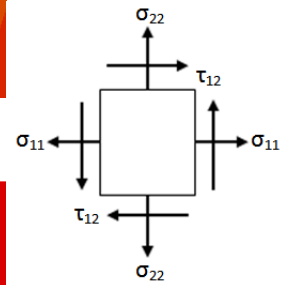
(a)



(b)



(c)



(d)

Figure 5-4: Contours of Normal Stress Distribution for Loads Equal to (a) 4N, (b) 56N, (c) 375N, (d) 2000N.

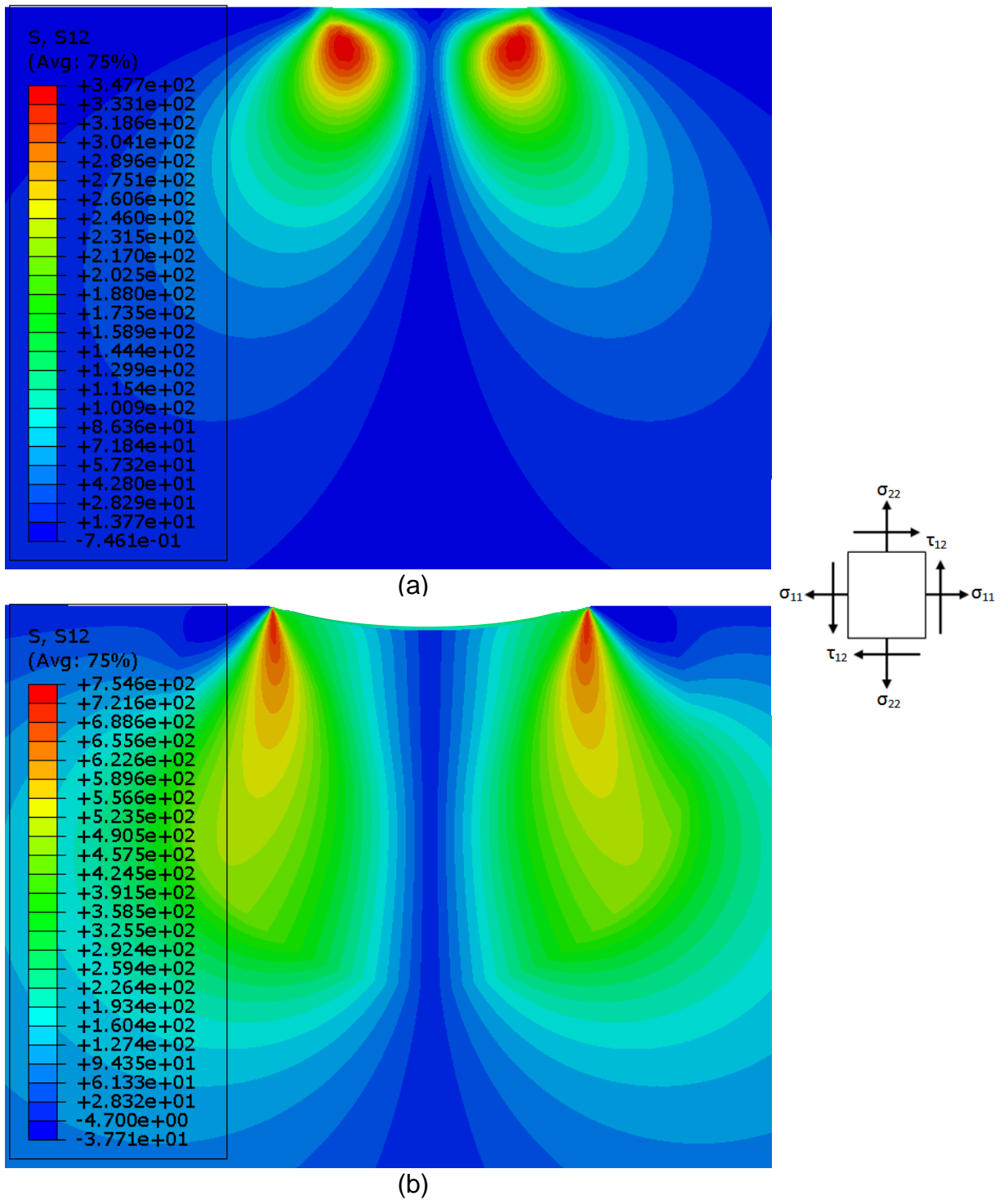


Figure 5-5: Contours of Shear Stress Distribution for Loads Equal to (a) 4N, (b) 2000N.

5.1.2 3D simulation

Next, 3D FEA simulation results are compared to the MMRI experimental results. The pin is firstly loaded for 1900N force, then the disk is rotated about 60 degrees at a temperature of 25°C, 150°C, 300°C, 500°C and 600°C. As mentioned in Section 5.1, the input values for FEA simulation are temperature, normal force and COF. The output values are torque and indentation diameter. Thus, for a given pair of pin and disk, the torque and the indentation diameter for both the experimental testing and FEA simulations are plotted against the interface temperature in Figure 5-6.

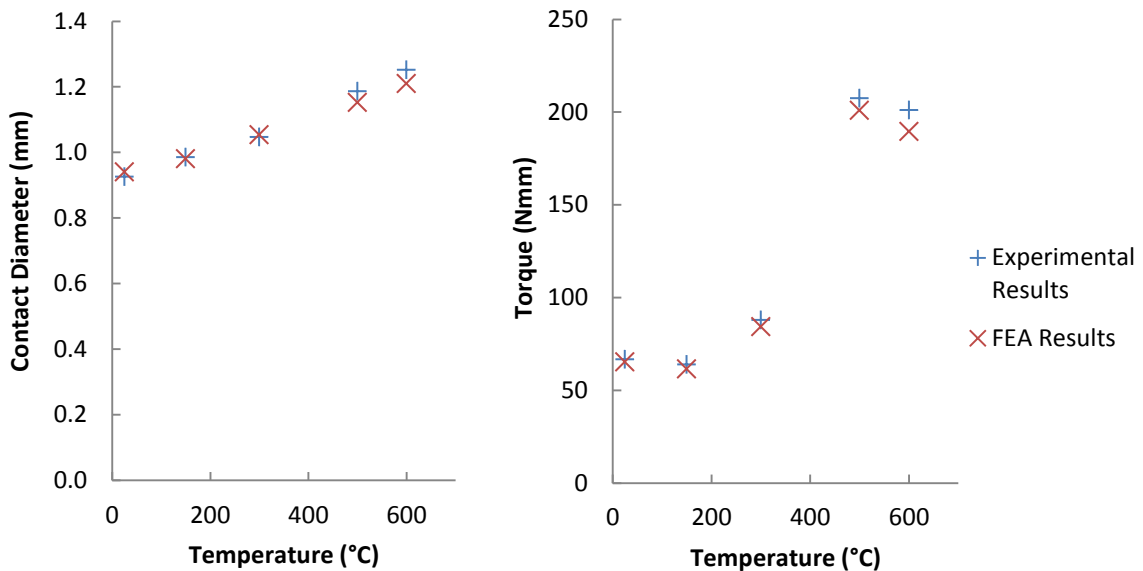


Figure 5-6: Contact Diameter and Torque at Different Temperature.

Due to the development of pile-up or sink-in, the contact diameter should be measured by taking the horizontal distance between the two sharp edges of the contact interface. As shown in Figure 5-6, the FEA results of the contact

diameter and torque agree well with the experimental results. Therefore, the 3D model is a reasonable representation of the entire tribometer setup at the MMRI. Note that under a constant normal load, the indentation diameter increases with increasing temperature as would be expected due to the thermal softening effects of the workpiece material.

The two shear stress components caused by the surface friction are plotted in Figure 5-7. Before the rotation of the pin, both of the two shear stress components are found to be close to zero. As the pin starts to rotate counter-clockwise, the surface friction causes both of the two shear stress components to increase. It has been found that the higher the surface friction, the larger the increase in the two shear stress components.

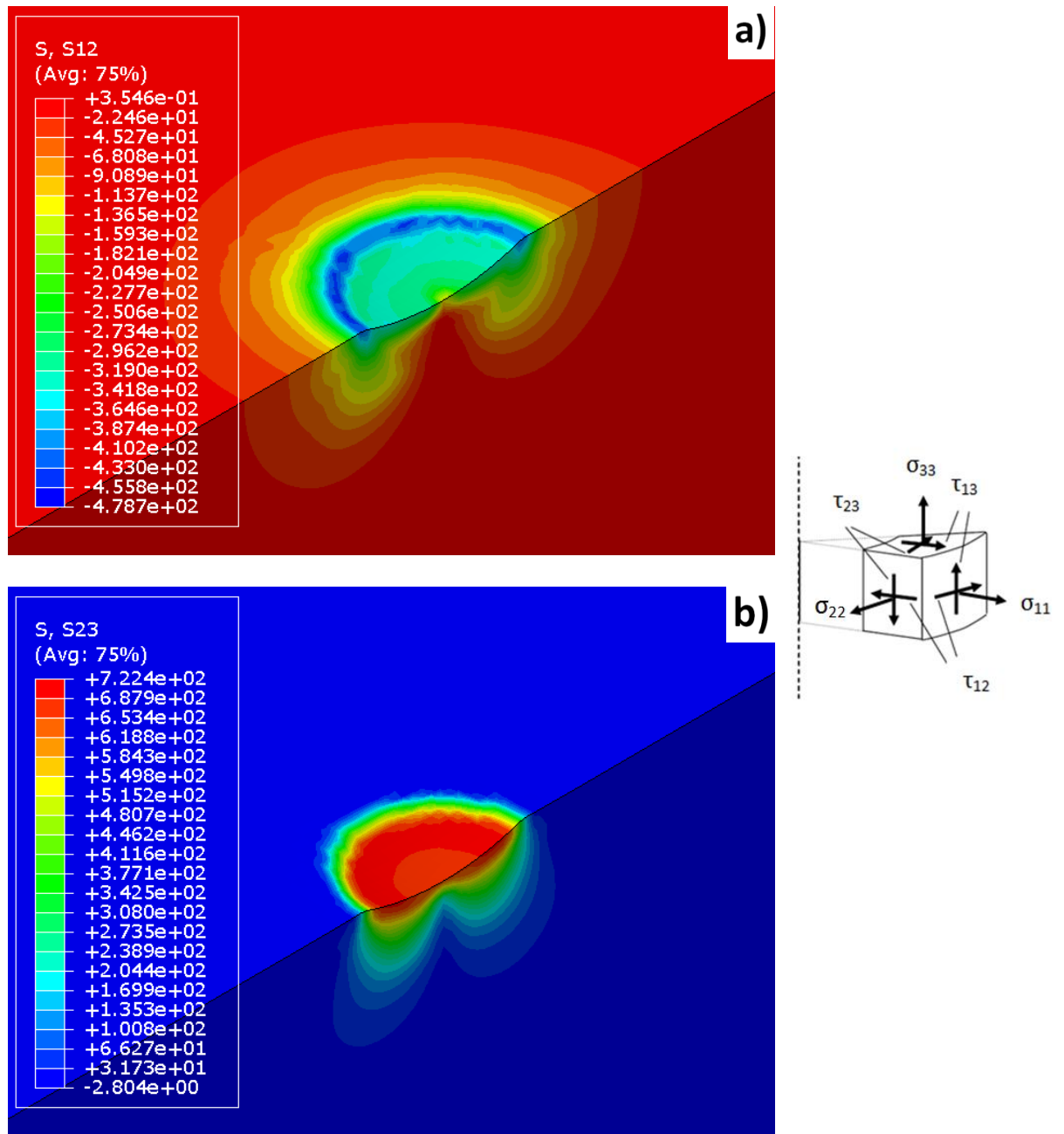


Figure 5-7: Shear Stress Distribution: (a) τ_{12} ; (b) τ_{23}

5.2 Boundary conditions effects

Further FEA simulations were performed in order to more accurately calculate the MMRI COF and explore other alternative testing methods. In this section, two different boundary conditions are tested separately during the rotational process of FEA simulation as shown in Figure 5-8. The first one is the force controlled boundary condition where the normal forces are kept constant during the rotation process (Figure 5-8a). The second one is the displacement controlled boundary condition where the indentation depths are fixed during the rotation process (Figure 5-8b).

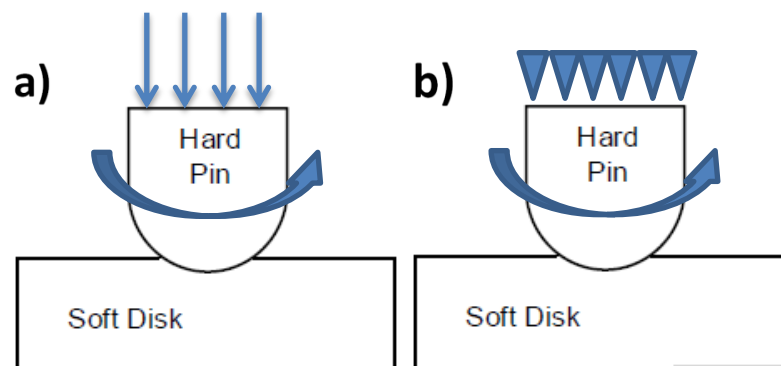


Figure 5-8: Two Boundary Conditions: (a) Force Control (b) Displacement Control.

5.2.1 Force controlled boundary condition

In order to evaluate the force controlled boundary condition, the disk is first loaded by a 2000N force, and then with the force kept constant, the pin is rotated for 60 degree about its own axis. This is the method that is currently used for the MMRI tribometer setup. Different COF values were tested to evaluate the friction effects on the output variables.

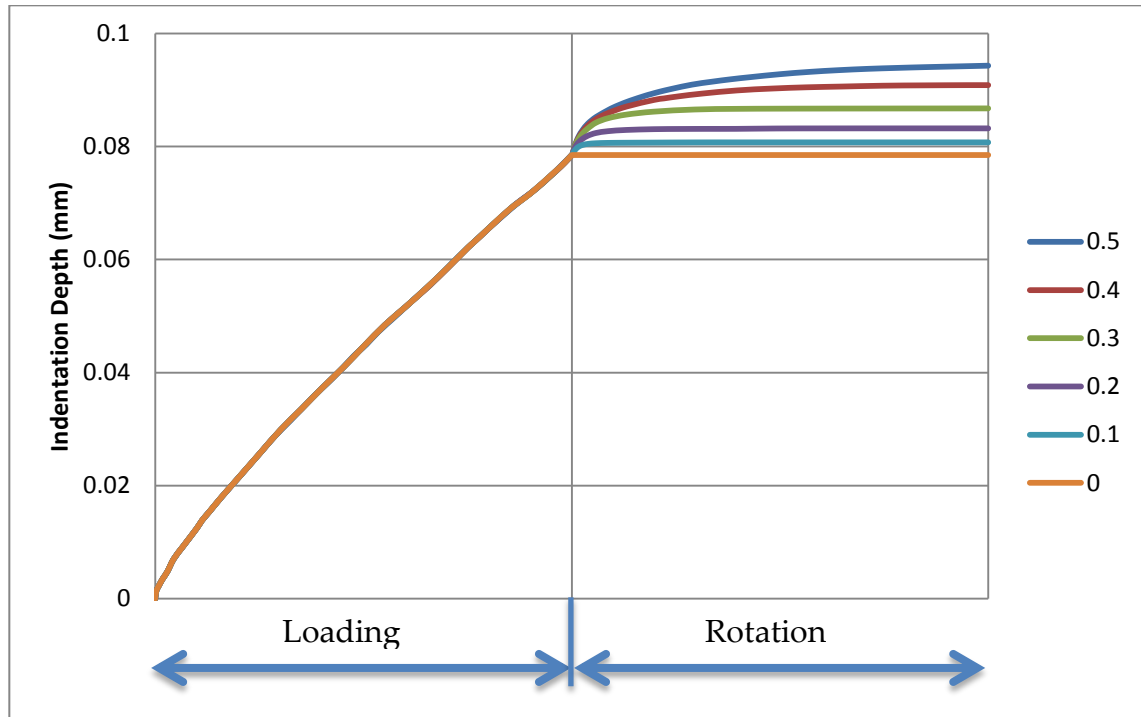


Figure 5-9: Indentation Depth Curve for Different Coefficients of Friction.

Indentation depth of the pin for different COF is plotted in Figure 5-9. Since the displacement of the pin is not fixed after the indentation process, one can see that the indentation depth increases during the rotation process. This is because the rotation of the pin will introduce a frictional shear stress at the surface, which increases the equivalent von Mises stresses and causes subsurface plastic deformation at the contact point. Thus, the indentation depth of the pin will increase during the rotation process. Also, it can be seen that the higher the COF, the larger the increase of indentation depth during the rotation process.

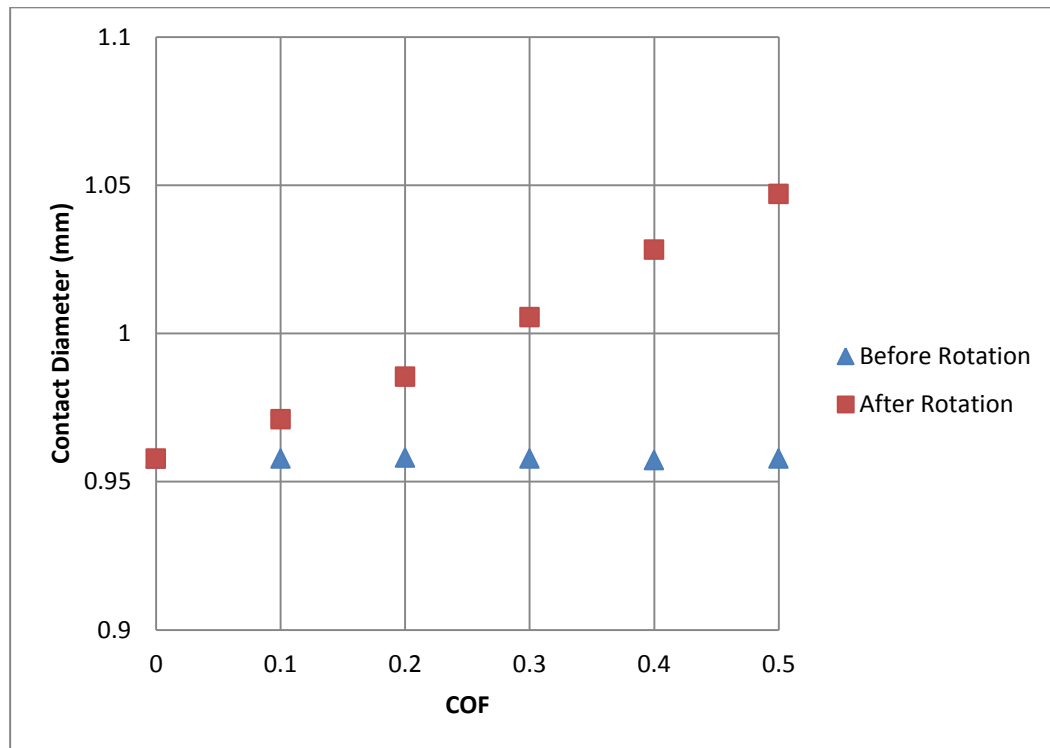


Figure 5-10: Contact Diameter Curve for Different Coefficients of Friction.

Contact diameters before and after rotation process under different COF are also measured and plotted in Figure 5-10. The triangular marks represent the contact diameter before rotation process under the constant load of 2000N. It is found that as the COF increases, the contact diameter remains relatively constant before rotation process. These observations are in agreement with the results obtained by Taljat and Pharr discussed in Section 2.3.1. They found that for strongly hardening materials ($n=0.5$), there is no discernable effect of friction on the indentation profile. Since the workpiece material in our FEA model is also a strongly hardening material ($n=0.45$), therefore the surface friction will not have a great impact on the contact diameter for indentation process.

On the other hand, the surface friction will affect the contact diameter during rotation process as shown by the squared mark in Figure 5-10. The contact diameter is found to increase as the surface friction increases. This is because the increase of surface friction increases the indentation depth, which then causes a larger contact area. As a result, the contact diameter increases during rotation process. Note that when the COF equals to zero, both the indentation depth and contact diameter does not change during the rotation process because there are no frictional shear stresses introduced by the rotation of the pin.

Although the COF is an input value in the FEA simulation, it could be recalculated by using the output variables generated by FEA simulation based on Equation (3). This recalculated COF could then be used to compare with the input COF for verifying the equation (3) derived by Biksa and examining which variables should be used for the COF calculation. In Figure 5-11, the rectangular mark represents the COF calculated using the contact diameter before rotation process and the triangular marks represent the COF calculated using the contact diameter after rotation. It is shown that the COF calculated using the contact diameter after rotation matches the input COF better than the one calculated using the indentation diameter before rotation. Thus, Equation (3) is verified and the COF should be calculated using the indentation diameter after the rotation process for MMRI experimental testing.

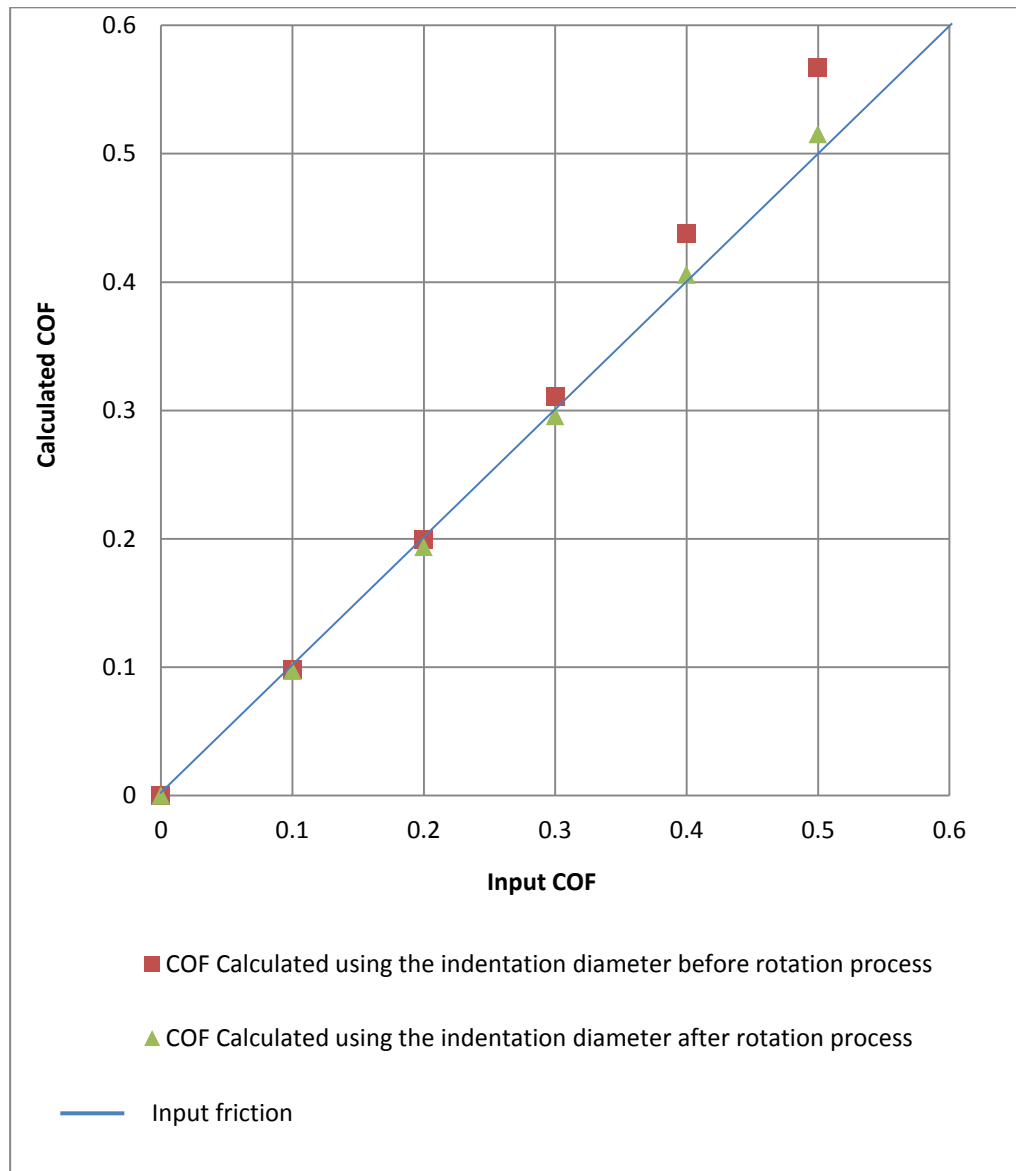


Figure 5-11: Coefficient of Friction Comparison.

5.2.2 Displacement controlled boundary condition

A displacement controlled boundary condition is not being used for the MMRI tribometer setup currently, but FEA simulations are performed to check the possibility of changing the MMRI tribometer setup and the accuracy of using

Equation (3) for this type of boundary condition. In the set of simulations, the disk is firstly loaded to a normal force of 2000N, and then with the displacement of the pin being held constant, the pin is rotated 60 degree about its axis. The normal force curves for different COF are plotted in Figure 5-12.

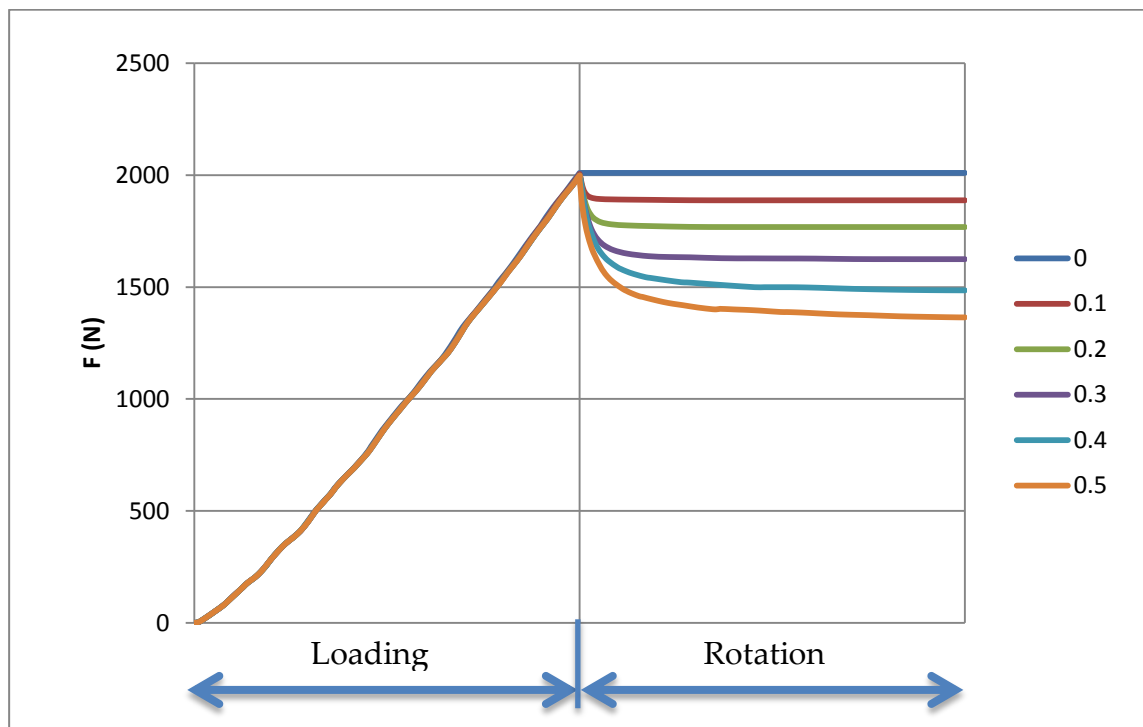


Figure 5-12: Normal Force Curve for Different Coefficient of Friction.

In this graph, depending on the contact COF, the normal force drop rapidly at the beginning and then maintains a constant value. This is caused by the sudden increase of frictional shear stress introduced by the rotating pin. According to the von Mises stress equation (9), when von Mises stress, hoop stress and radial stress are remained relatively constant, the normal stress will decrease rapidly with the sudden increase in the frictional shear stress during the rotation process, which will then cause the decrease in the normal load. Once the

frictional shear stress reaches a limit, then normal stress or the normal load will be maintained at a constant value. This graph also shows that the higher the COF, the larger the drop in the normal force during rotation.

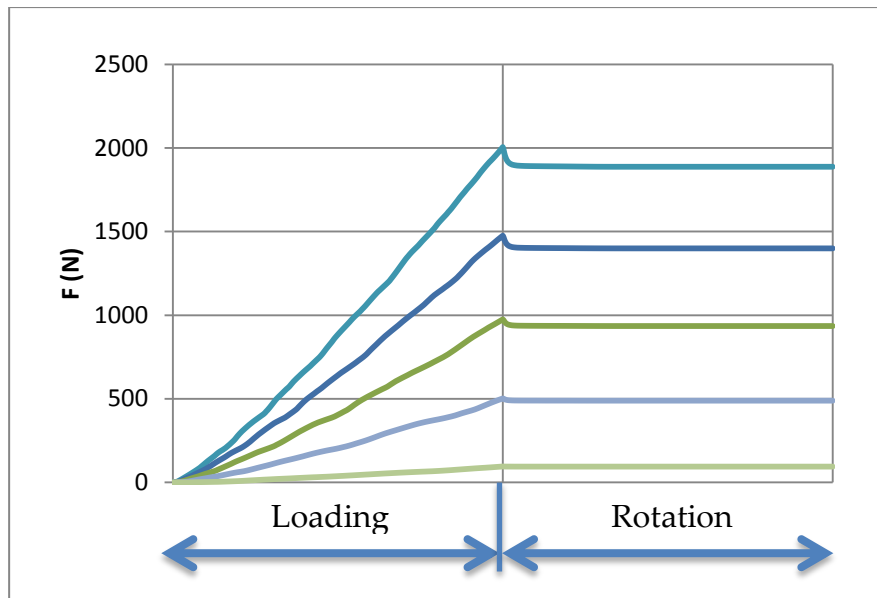


Figure 5-13: Normal Force Curve for Different Indentation Depth.

Simulations of friction effects on initial loading force are also performed and plotted in Figure 5-13. In this set of simulations, the disk is loaded with different initial force before the rotation process, and then as the pin starts to rotate, the loading force is expected to decrease. From this graph, it is shown that the higher the initial normal force during the indentation process, the larger the drop in normal force during rotation.

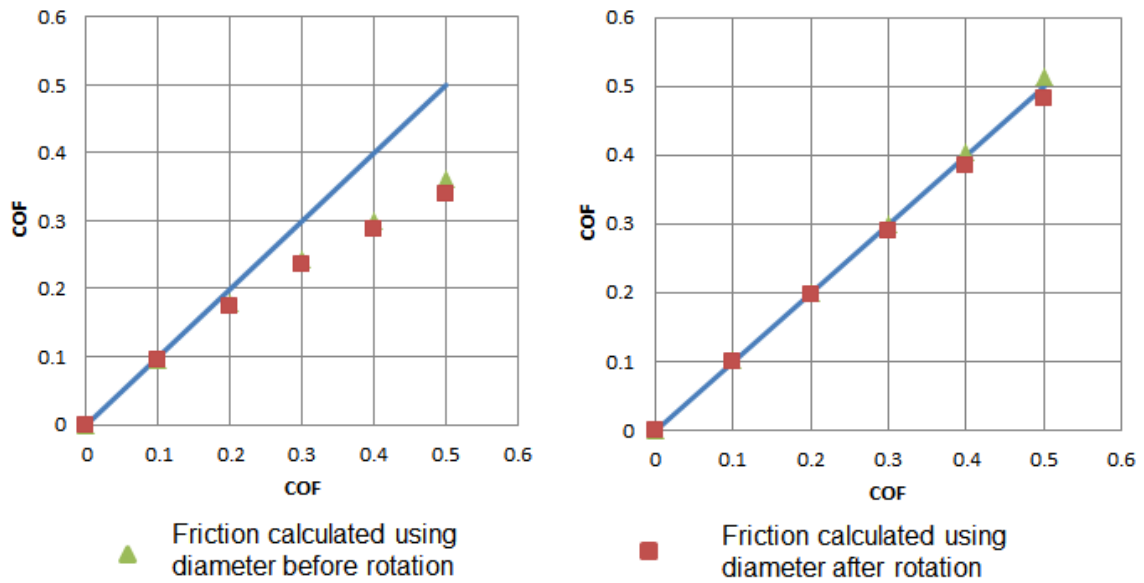


Figure 5-14: Friction Calculated Using the Force (a) Before Rotation (b) After Rotation.

Finally, similar to the force controlled boundary condition, the calculated COF is compared with the input COF for the displacement controlled boundary condition. Figure 5-14(a) is the COF calculated using the force before rotation and Figure 5-14(b) is the COF calculated using the force after rotation. By comparing these two graphs, it could be seen that the force after the rotation process should be used in Equation (3) for calculating the COF. Also, when the contact diameter is taken into consideration, Figure 5-14 shows that contact diameter does not have a great impact on the calculation of COF. Therefore, the MMRI COF equation is valid for the displacement controlled boundary condition test and it provides us another alternative experimental testing method for use in the future.

5.3 Temperature effects

Interface temperature also has a great impact on the results. Figure 5-15 shows how the temperature affects the indentation depth during heating and the rotation process for a friction coefficient of 0.2. A forced controlled boundary condition is applied to this FEA model. During the heating process, the increase in interface temperature softened the disk material, which caused a slight increase in the indentation depth. When the interface temperature is at 400°C, the indentation depth at the end of the heating process is 0.082mm, which is higher than the case of the 200°C interface temperature, and lower than the case of the 600°C interface temperature. Therefore, the higher the interface temperature, the higher the increase of the indentation depth during the heating process. During rotation, similar to the forced control boundary condition discussed in Section 5.2.1, the increase in the frictional shear stress caused the von Mises stress at the contact surface to increase, resulting in an increase in the indentation depth. The graph also shows that the higher the interface temperature, the higher the increase in the indentation depth during rotation. Therefore, when the COF is the same, a higher interface temperature will cause a larger increase in the indentation depth during both heating and rotation.

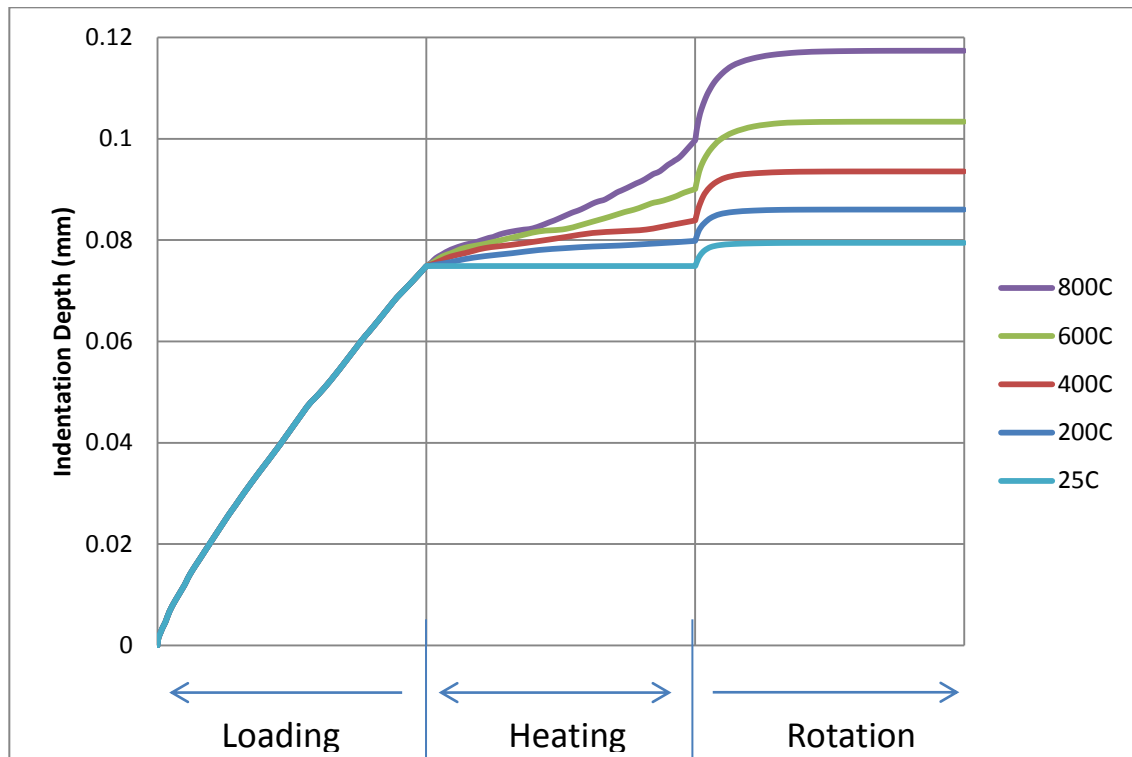


Figure 5-15: Indentation Depth curve during Loading, Heating and Rotation Process.

Figure 5-15 shows the interface temperature effects on the mean normal stress, mean shear stress and contact diameter under constant load and constant friction coefficient. As shown in Figure 5-16(a) and (b), both mean normal (σ) and mean shear stress (τ) decrease as the interface temperature increases. This analytically verified that when the load and surface friction is constant, an increase of interface temperature will cause both the normal and shear stress to decrease. Also, in Figure 5-16(c), the contact diameter, D_{ind} , increases with an increase in interface temperature as would be expected due to the thermal softening of the workpiece material.

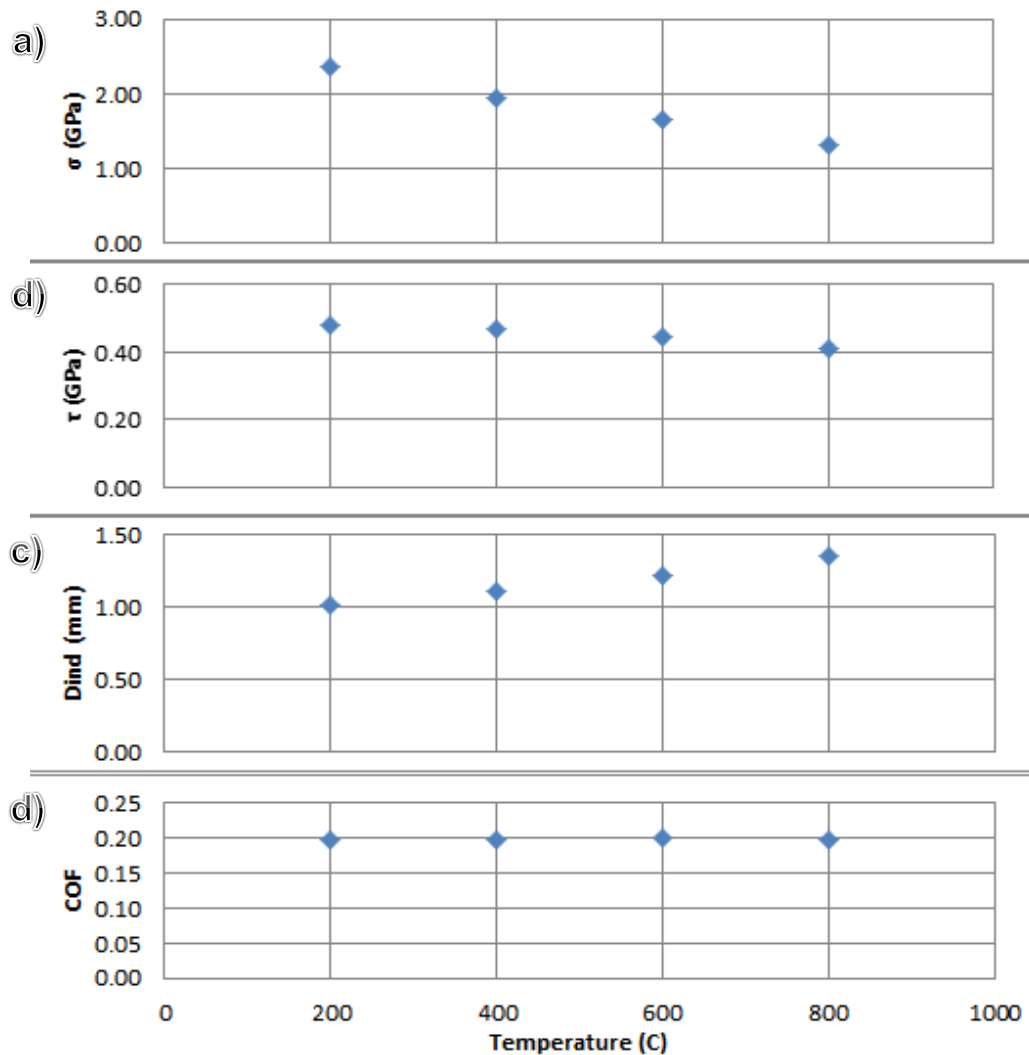


Figure 5-16: FEA results for friction coefficient of 0.2.

The input COF for this set of simulations is kept constant at 0.2. The recalculated COF obtained based on the indentation diameter after rotation is plotted against the interface temperature in Figure 5-16(d). It can be seen that the calculated COF agrees well with the input COF at various interface temperatures. Thus, it is suggested that the MMRI COF should be calculated using the diameter after rotation regardless of whether heat is added to the system.

5.4 Soft pin indenting on hard disk

Due to the difficulty and cost in forming a spherical tipped pin with tooling materials, such as diamond and ceramics, it is important to examine the possibility of the material reversal for MMRI tribometer friction testing with the pin being the workpiece material and the disk being the tooling material. Thus, a preliminary 3D FEA model of a soft pin indenting on a rigid disk was developed. The pin is modeled as an elastic-plastic body and the disk is modeled as a rigid body. The whole model is composed of 102257 nodes and 97039 C3D8R elements. Figure 5-17 shows that when a 1900N normal force is applied on the soft pin, the normal stress is well distributed along the interface and the maximum normal stress is around 2.6GPa.

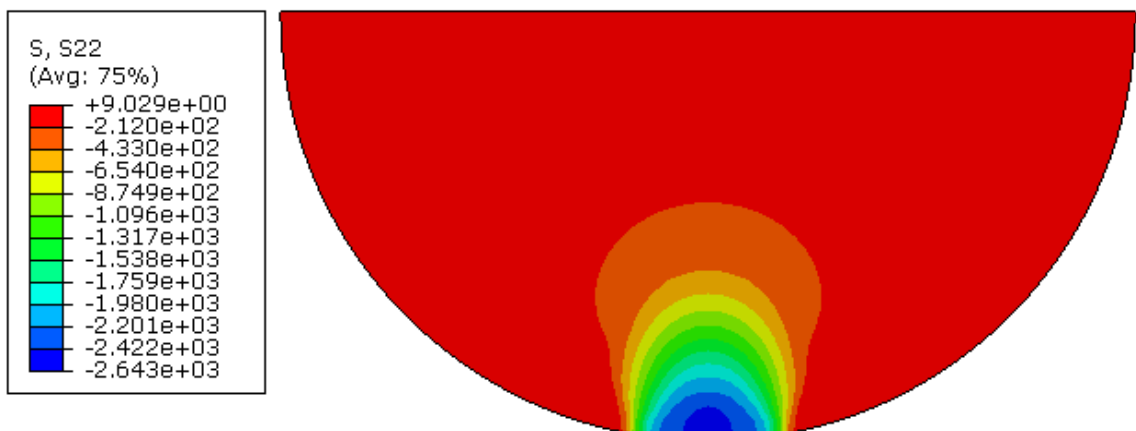


Figure 5-17: Normal Stress Distribution.

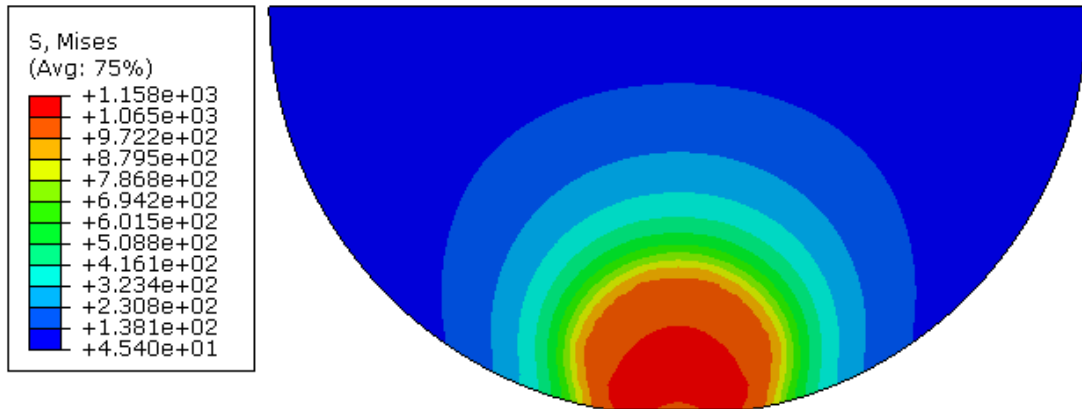


Figure 5-18: Von Mises Stress Distribution.

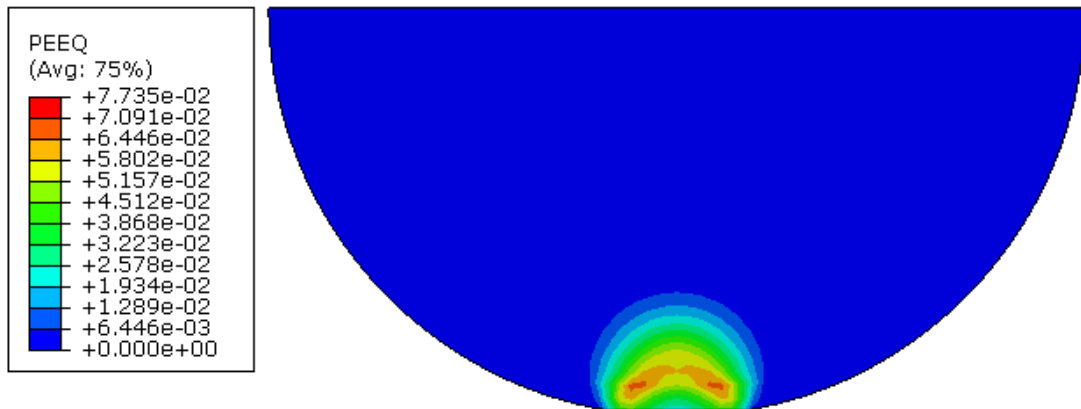


Figure 5-19: Equivalent Plastic Strain Distribution.

Figure 5-18 and 5-19 show the von Mises stress and equivalent plastic strain distribution inside the pin, respectively. It can be seen that both the maximum von Mises stress and the maximum plastic deformation occur inside the pin. Force and displacement controlled rotation process are also examined for the case of the soft pin indenting on a hard disk. Figure 5-20 shows that the calculated COF for both the force and displacement controlled rotation process match each other well. Thus the material reversal of the soft pin on hard disk is

reliable for experimental testing in MMRI, and Equation (3) is valid for this type of operating condition.

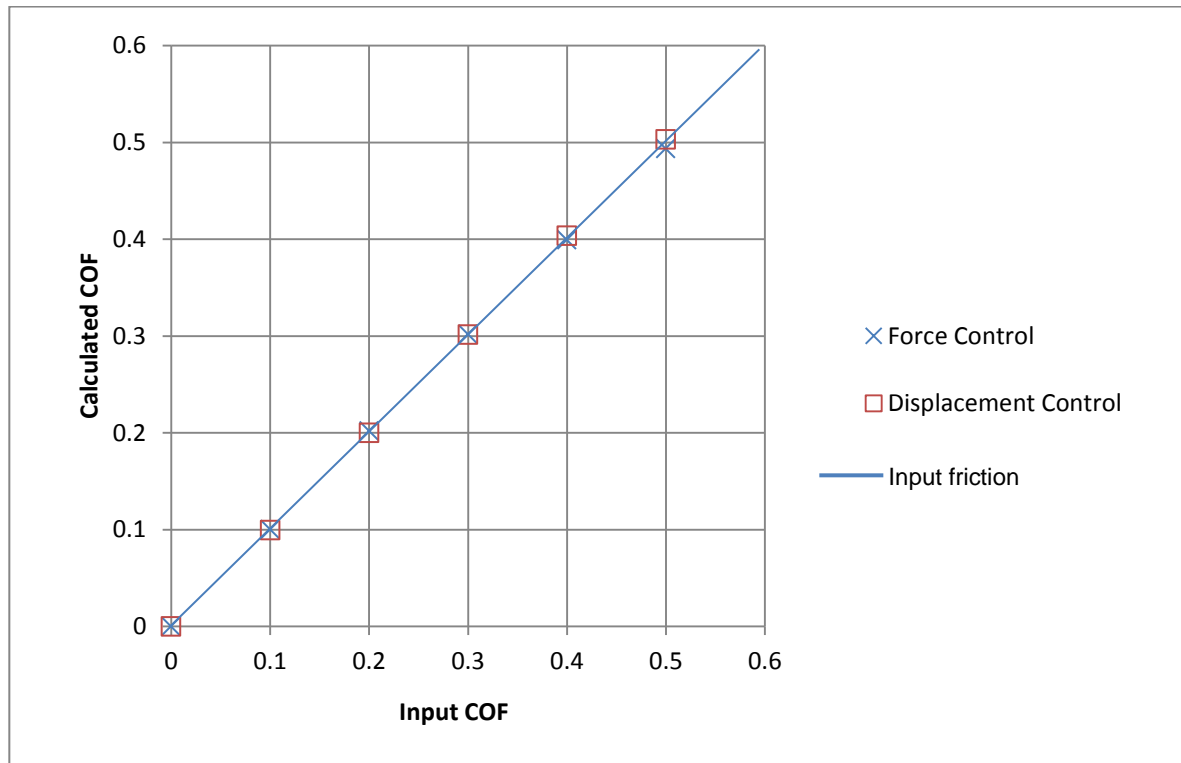


Figure 5-20: Calculated COF vs. Input COF.

Chapter 6. Conclusions

FEA simulations of the MMRI tribometer were performed and compared with experimental results. It was shown that the FEA results match the experimental results well, which validates the equation used to calculate the COF for MMRI tribometer. Three different operation conditions were simulated in order to more accurately calculate the MMRI COF value and improve its ability to simulate the machining environment. Our results show that the MMRI COF equation is valid for both the force and the displacement controlled boundary condition friction test and it should be calculated using the force after rotation for a displacement controlled rotation process and using the contact diameter after rotation for a force controlled rotation process. Also, in order to reduce the cost of the tribometer test, it has been shown that the COF equation derived by Biksa can be used for calculating the friction between a soft pin indenting on a hard disk in the experiment.

Since the FE model results agree with the experimental results, once a COF is experimentally obtained from the MMRI tribometer, it could be then inputted into the FE model to check the indentation diameter and reaction torque. Also, since the FE model is able to generate detailed stress, strain and temperature distribution as well as indentation profile at the contact surface during different process, it could be used as an assistive tool for the setting up the MMRI tribometer and ensuring that critical conditions are achieved.

Chapter 7. Future Work

- Perform more detailed numerical simulations on soft pin indenting on hard disk case with different interface temperature in order to evaluate the temperature effects on the calculation of friction.
- Surface roughness is not considered in the FEA model, therefore, a model involving asperity contact between the pin and disk could be built in order to include the effects of different surface roughness.
- Model the pin as an elastic-plastic body in order to obtain the stress and strain distribution inside the pin for a 3-Dimensional view.
- Carry out FEA simulations on other workpiece materials in order to see the effects of material properties on the FEA results.
- Build a complete list of material properties for different workpiece materials so that the FEA model could be used as an assistive tool to obtain the stress and strain distribution during the experimental testing of coefficient of friction on the MMRI tribometer.
- Carry out FEA simulations for different rotational speeds of the pin in ABAQUS explicit in order to examine the effects of the strain rate term in the Johnson-Cook equation.
- Study and include wear models into the system in order to examine the influence of temperature, friction, sliding speed and compressive stress on wear.

Chapter 8. Bibliography

ABAQUS User's Manual, Version 6.9, (2009) ABAQUS Inc., Providence, Rhode Island, USA

Akyuz, F.A., & Merwin, J.A., (1968). "Solution of Non-linear Problems of Elastoplasticity by Finite Element Method", *J. AIAA*, 6.

Antunes, J.M., Menezes, L.F., & Fernandes, J.V., (2006). "Three-Dimensional Numerical Simulation of Vickers Indentation Tests", *International Journal of Solids and Structures*, 43, 784-806.

Biksa, A., Yamamoto, K., Dosbaeva, G., Veldhuis, S.C., Fox-Rabinovich, G.S., Elfizy, A., Wagg, T., & Shuster, L.S., (2010), "Wear Behavior of Adaptive Nano-multilayered AlTiN/MeN PVD Coatings during machining of Aerospace Alloys", *Tribology International*, 43, 1491-1499.

Biksa, A. (2010). Tribological Characterization of Surface Engineered Tooling for Metal Cutting Applications. Open Access Dissertations and Theses, 4325-4508.

Bhushan, B., (1996). Tribology and Mechanics of Magnetic Storage Devices, Second Edition, Springer-Verlag, New York.

Boothroyd, G. (1975). *Fundamentals of Metal Machining and Machine Tools*. Scripta Book Company, 85.

Bowden, F., & Tabor, D. (1950). *The Friction and Lubrication of Solids*. Oxford University Press.

Bowden, F., & Tabor, D. (1939). "The Area of Contact between Stationary and between Moving Surfaces", *Proceeding of the Royal Society of London*. 391-413

Care, G., & Fischer-Cripps, A.C. (1997). "Elastic-plastic Indentation Stress Fields using the Finite-Element Method." *Journal of Materials Science*, 32, 5653-5659.

Djabella, H., & Arnell, R.D. (1992). "Finite Element Analysis of the Contact Stresses in an Elastic Coating on an Elastic Substrate", *Thin Solid Films*, 213, 205-219

- Djabella, H., & Arnell, R.D. (1993). "Finite Element Comparative Study of Elastic Stress in Single, Double Layer and Multilayered Coated Systems". *Thin solid films*, 235, 156-162
- Dorogoy, A., & Rittel, D. (2009). "Determination of the Johnson-Cook Material Parameters using the SCS specimen", *Experimental Mechanics*, 49, 881-885.
- Feng, G., Qu, S., Huang, Y., & Nix, W.D. (2007). "An Analytical Expression for the Stress Field Around an Elastoplastic Indentation/Contact", *Acta Materialia*, 55, 2929-2938.
- Friedrich, K., Goda, T., Varadi, K., & Wetzel, B., (2004). "Composites Produced by a Sliding Indentor: Part I- Normally Oriented Fibers", *Journal of Composite Materials*, 38, 1583-1606.
- Fox-Rabinovich, G.S., Veldhuis, S.C., Scvortsov, V.N., Shuster, L.S., Dosbaeva, G.K., & Migranov, M.S. (2004). "Elastic and Plastic Work of Indentation as a Characteristic of Wear Behaviour for Cutting Tools with Nitride PVD Coatings", *Thin Solid Films*, 469, 505-512.
- Green, A.E. (1949). "On Boussinesq's problem and penny-shaped cracks", *Proc Cambridge Philos Soc*, 45, 251.
- Ghosh, A., & Malik, A.K. (1985), *Manufacturing Science*, Affiliated East West Press, New Delhi, 191-192.
- Hamilton, G.M., & Goodman, L.E., (1966). "Stress Field Created by a Circular Sliding Contact, *Journal of Applied Mechanics*", 33, 371-376.
- Hardy, C., Baronet, C.N., & Tordion, G.V., (1971). "Elastoplastic Indentation of a Half Space by a Rigid Sphere", *Journal of Numerical Methods in Engineering*, 3, 451-462.
- Hertz, H.R., (1882). "On Contact Between Elastic Bodies", *Collected Works*, 1
- Heilmann, P., Don, J., Sun, T.C., & Rigney, D.A. (1983). "Sliding Wear and Transfer", *Wear*, 91, 171-190.
- Holmberg, K., Laukkanen, A., Ronkainen, H., Wallin, K., Varjus, S., & Koskinen, Jari., (2006). "Tribological Contact Analysis of a Rigid Ball Sliding on a Hard Coated Surface Part I: Modelling Stresses and Strains". *Surface & Coatings Technology*. 200, 3793-3809.

- Jackson, R.L., & Green, I., (2005). "A Finite Element Study of Elasto-plastic Hemispherical Contact against a Rigid Flat", *Journal of tribology*, 127, 343-354.
- Jungk, J.M., Michael, J.R., & Prasad, S.V., (2008). "The Role of Substrate Plasticity on the Tribological Behavior of Diamond-Like Nanocomposite Coatings", *Acta Materialia*, 56, 1956-1966.
- Johnson, K.L., & Jefferis, J.A. (1963). "Plastic Flow and Residual Stresses in Rolling and Sliding Contact" *Mech. Eng. Symp. on Rolling Contact Fatigue*, 54
- Johnson, K.L., (1985). *Contact Mechanics*, Cambridge University Press, Cambridge.
- Kim, H.S., (2001). "Finite Element Analysis of High Pressure Torsion Processing", *Journal of Materials Processing Technology*, 113, 617-621.
- King, R.B., & O'Sullivan, T.C. (1987). "Sliding Contact Stresses in a Two-dimensional Layered Elastic Half-space". *International Journal of Solids and Structures*, 23, 581-597.
- Kral, E.R., Komvopoulos, K., & Bogy, D.B. (1993). "Elastic-plastic Finite Element Analysis of Repeated Indentation of a Half-space by a Rigid Sphere" *Journal of applied mechanics*, 60, 829-841.
- Komvopoulos, K., (1989). "Finite Element Analysis of a Layered Elastic Solid in Normal Contact with a Rigid Surface", *Journal of Tribology*, 110, 477-485.
- Komvopoulos, K., & Gong, Z.Q. (2007), "Stress Analysis of a Layered Elastic Solid in Contact with a Rough Surface Exhibiting Fractal Behaviour". *International Journal of Solids and Structures*. 44, 2109-2129.
- Korotkov, V., Shuster, L., & Zelin, M. (1997) "Wear Resistance of Die Steel under Conditions of Hot Sliding Friction." *Material Science and Heat Treatment*, 39, 57-60.
- Kucharski, S., & Mroz, Z. (2001) "Identification of Plastic Hardening Parameters of Metals from Spherical Indentation Tests", *Materials science and engineering*. 318, 65-76.
- Lee, W.S., & Lin, M.T. (1997), "The Effects of Strain Rate and Temperature on the Compressive Deformation Behaviour of Ti-6Al-4V Alloy", *Journal of Materials Processing Technology*, 71, 235-246.

- Lee, H, Lee, J. H., & Pharr, G.M., (2005), “A Numerical Approach to Spherical Indentation Techniques for Material Property Evaluation” *Journal of the Mechanics and Physics of Solids*, 53, 2037-2069.
- Luo, J., Li, M., Yu, W., Li, H., (2010), “The Variation of Strain Rate Sensitivity Exponent and Strain Hardening Exponent in Isothermal Compression of Ti-6Al-4V Alloy”, *Material and Design*, 31, 741-748.
- Mata, M., Casals, & O., Alcala, J. (2006), “The Plastic Zone Size in Indentation Experiments: The Analogy with the Expansion of a Spherical Cavity”, *International Journal of Solids and Structures*, 43, 5994-6013.
- Marsh, D.M., (1964). “Plastic Flow in Glass.” *Mathematical and Physical Sciences*, 420-435.
- Mikhin, N.M., & Lyapin, K.S. (1971). “Influence of a Perpendicular load and the Diameter of the Indenter on the Tangential Strength on the Adhesive Bond” *Fiziko-Khimicheskaya Mekhanika Materialov*, 7, 34-38.
- Michau, B., Berthe, D., & Godet, M., (1974), “Influence of Pressure Modulation in a Linear Hertzian Contact on the Internal Stress-Field”, *Wear*, 28, 187-195.
- Moore, A.J.W., (1948), “Deformation of Metals in Static and in Sliding Contact”, *Mathematical and physical sciences*, 231-244.
- Morton, W.B., & Close, L.J., (1922), “Notes on Hertz’s theory of Contact Problems”, *Philos Mag.* 43, 320-329.
- Nowell, D., & Hills, D.A., (1988), “Contact Problems Incorporating Elastic Layers”, *International journal of Solids and Structures*, 24, 105-115.
- Ozel, T., & Zeren, E., (2006), “A Methodology to Determine Work Material Flow Stress and Tool-Chip Interfacial Friction Properties by Using Analysis of Machining”. *Journal of Manufacturing Science and Engineering*, 529-537.
- Patton, S.T., & Zabinski, J.S., (2002). “Advanced Tribometer for in situ Studies of Friction, Wear and Contact Condition-advanced Tribometer for Friction and Wear Studies”. *Tribology letter*, 13, 263-273.
- Rabinowicz, Ernest (1995). *Friction and Wear of Materials*. Wiley, 25.
- Rigney, D.A., Hirth, J.P., (1979). “Plastic Deformation and Sliding Friction of Metal”. *Wear*, 53, 345-370.

- Podra, P., & Andersson, S., (1999), "Simulating Sliding Wear with Finite Element Method", *Tribology International*, 32, 71-81.
- Schey, J., (1983). *Tribology in Metalworking*. Waterloo: American Society for Metals, 581.
- Scheibert, J., Prevost, A., Debrégeas, G., Katzav, E., Adda-Bedia, M., (2009) "Stress Field at a Sliding Frictional Contact: Experiments and Calculations", *Journal of the Mechanics and Physics of Solids*, 57, 1921.
- Schwarzer, N., Richter, F., & Hecht, G., (1999), "The Elastic Field in a Coated Half-space Under Hertzian Pressure Distribution". *Surface and Coatings Technology*, 114, 292-303.
- Sen, S., Aksakal, B., & Ozel, A., (1998). "A Finite-Element Analysis of the Indentation of an Elastic-work Hardening Layered Half-space by an Elastic Sphere", *International Journal of Mechanical Sciences*, 40, 1281-1293.
- Seo, S., Min, O., & Yang, H., (2005). "Constitutive Equation for Ti-6Al-4V at High Temperature Measured Using the SHPB Technique." *International Journal of Impact engineering*. 31, 735-754.
- Shaw, M.C., Ber, A., & Mamin, P.A., (1960), "Friction Characteristics of Sliding Surfaces Undergoing Subsurface Plastic Flow." *Journal of Basic engineering*, 82, 342-346.
- Shaw, M.C., (2005) "Metal Cutting Principles 2nd Ed". Oxford Series on Advanced Manufacturing. 235.
- Shirakashi, T., Komanduri, R., & Shaw, M.C., (1978). "On Friction and Metal Transfer of Sliding Surfaces Undergoing Subsurface Plastic Deformation." *Wear*, 48, 191-199.
- Shrot, A., & Baker, M.(2011), "Determination of Johnson-Cook Parameters From Machining Simulations", *Computational Materials Science*, 52, 298-304.
- Tabor, D., (1986). "Indentation Hardness and its Measurement: Some cautionary comments", *Microindentation Techniques in Materials Science and Engineering*, 129-158.
- Taljat, B., & Pharr, G.M., (2004). "Development of Pile-up During Spherical Indentation of Elastic Plastic Solids". *International Journal of Solids and Structures*. 41, 3891-3904.

- Tian, H., & Saka, N.,(1992) “Finite Element Analysis of Interface Cracking in Sliding Contacts”. *Wear*, 155, 163-182.
- Trent, Edward M., & Wright, Paul K. (2000) *Metal Cutting*. 4th. Butterworth-Heinemann.
- Valiorgue, F., Rech, J., Hamdi, H., Bonnet, C., Gilles, P., & Bergheau, J.M.,(2008) “Modelling of Friction Phenomena in Material Removal Processes”, *Journal of Material Processing Technology*, 201, 450-453.
- Xue, Q., Meyers, M.A., & Nesterenko, V.F. (2002) “Self-organization of Shear Bands in Titanium and Ti-6Al-4V Alloy”, *Acta Materialia*, 50, 575-596.
- Ye, N., & Komvopoulos, K., (2003), “Effect of Residual Stress in Surface Layer on Contact Deformation of Elastic-plastic Layered Media”, *Journal of Tribology*, 125, 692.
- Yin, X., & Komvopoulos, K., (2010) “An Adhesive Wear Model of Fractal Surfaces in Normal Contact”, *International Journal of Solids and Structures*, 47, 912-921.
- Zorev, NN. (1963). “Interrelationship Between Shear Processes Occurring Along Tool Face and on Shear Plane in Metal Cutting.” *Engineering Research Conference*, 42-49.